RSC Advances

PAPER

View Article Online
View Journal | View Issue

Cite this: *RSC Adv.*, 2026, **16**, 2342

Design, synthesis, biological evaluation, and *in silico* studies of novel 1,3-thiazole derivatives

Nguyen Duy Khanh,[a] Nguyen Thi Hong Anh,[b] Nguyen Van Son,[a] Nguyen Thi Mai Tho,[a] Nguyen Thi Nhat Thang,[a] Tran Thuy Quyen[a] and Tran Nguyen Minh An *[a]

A series of novel 1,3-thiazole heterocyclic derivatives has been synthesized and structurally characterized using melting point, FT-IR, 1D and 2D NMR, and HR-MS. The compounds were screened for antibacterial activities, three human cancer cell lines (A549, HepG2, and MCF-7), and anti-inflammatory and α-glucosidase inhibitory activities, utilising MIC, MTT, α-glucosidase inhibitory, and NO assays, respectively. Entry **4e** exhibited the most potent antibacterial activity (MIC = 83.5 μM). Entry **4g** exhibited significant inhibitions against three cancer cell lines: MCF-7, HepG2, and A549 (IC_{50} = 2.6–6.6 μM). Entry **4f** exhibited significant anti-inflammatory activity (IC_{50} = 15.4 ± 1.0 μM), comparable to the dexamethasone drug (IC_{50} = 13.7 ± 1.2 μM). Notably, **4a** and **4l** exhibited potent α-glucosidase inhibitory activity (IC_{50} = 46 ± 2 μM and 41 ± 2 μM, respectively), surpassing acarbose (IC_{50} = 117 ± 8 μM). Molecular docking studies revealed energetically favourable interactions between the ligands and the active sites of the target enzymes, in good agreement with the predicted biological activities obtained from *in silico* analyses. A 100 ns molecular dynamics simulation of the **4l-4J5T** complex further confirmed its structural stability after 60 ns, with key residues Glu428 and Asn452 maintaining hydrogen bond interactions for approximately 80% of the simulation time. In addition, ADMET predictions indicated that compound **4l** possesses favourable pharmacokinetic properties. Collectively, these findings highlight a novel thiazole-based scaffold exhibiting multi-target biological activity and underscore its promising potential for further drug development.

Received 4th November 2025
Accepted 29th December 2025

DOI: 10.1039/d5ra08472e

rsc.li/rsc-advances

1. Introduction

Thiazole is a sulfur- and nitrogen-containing five-membered heterocycle known for broad pharmacological significance. Thiazole derivatives have demonstrated antibacterial,[1] anti-inflammatory,[2] anticancer,[3] and antidiabetic effects,[4] owing to their strong ability to interact with target enzymes and receptors.[5,6] Clinically approved thiazole-containing drugs, including the thiazolidinediones pioglitazone and rosiglitazone, highlight the therapeutic importance of this scaffold in type-II diabetes management through peroxisome proliferator-activated receptor gamma (PPARγ) activation and subsequent enhancement of insulin sensitivity.[7–10]

Carbazole is a tricyclic aromatic system found in natural and synthetic bioactive molecules.[11] Its rigid π-conjugated framework and favourable electronic properties enable interactions with diverse biological targets.[12–15] Carbazole derivatives have been widely reported to show anticancer, anti-inflammatory, antioxidant, antimicrobial, neuroprotective, and antidiabetic properties, underscoring their pharmacological versatility.[16] Carvedilol, a U.S. Food and Drug Administration (FDA)-approved carbazole-based β-blocker, further exemplifies the clinical relevance of this scaffold, also demonstrating beneficial effects on insulin sensitivity and glucose regulation.[17,18] Recent investigations have shown that carbazole derivatives may modulate key diabetic targets, including α-glucosidase, dipeptidyl peptidase-4 (DPP-4), and PPARγ, supporting their potential in the treatment of type 2 diabetes.[19–21] Given the established bioactivity of thiazole and carbazole systems, the hybridisation of both motifs represents a rational approach to generate multifunctional therapeutic scaffolds. Recent studies have reported carbazole–thiazole hybrids with promising activity profiles, reinforcing the attractiveness of this strategy. Several studies, such as those by Krawczyk *et al.* (2024), Marufa *et al.*, Çapan *et al.*, and Donarska *et al.* (2025), have reported hybrid derivatives with promising *in vitro* and *in silico* activities.[22–25]

Bacterial replication and cell-wall integrity depend on DNA gyrase, topoisomerase IV, and β-lactamase. Potent antibacterial agents often employ planar aromatic frameworks or metal-binding heterocycles to disrupt these catalytic systems.[26]

[a]*Faculty of Chemical Emgineering (FCE), Industrial University of Ho Chi Minh City (IUH), 12 Nguyen Van Bao, Hanh Thong Ward, Ho Chi Minh City, Vietnam. E-mail: trannguyenminhan@iuh.edu.vn*

[b]*Faculty of Chemical Engineering, Ho Chi Minh City University of Industry and Trade, 140 Le Trong Tan Street, Tay Thanh Ward, Ho Chi Minh, 70000, Vietnam*

Tyrosine kinases, tubulin, and topoisomerases regulate cancer proliferation. Carbazole provides a rigid π-surface for DNA and protein interactions, whereas thiazole introduces polarity and facilitates the orientation of H-bonding. Their hybrid enables complementary hydrophobic and polar contacts, supporting its promise as an anticancer scaffold.[27] Inducible nitric oxide synthase (iNOS) mediated nitric oxide production drives chronic inflammation. Ligands with π-rich skeletons and heteroatom donors can engage the heme centre and L-arginine pocket, enabling efficient iNOS modulation.[28] α-Glucosidase regulates carbohydrate breakdown and postprandial glucose levels. Heterocycle-bearing ligands mimic substrate interactions. Thiazole substitution enhances polarity and binding orientation, highlighting relevance for glycaemic modulation.[29] Based on this rationale, we designed, synthesised, and examined a series of previously unreported 1,3-thiazole derivatives. The compounds underwent comprehensive characterisation through Fourier transform infrared spectroscopy (FT-IR), nuclear magnetic resonance spectroscopy (NMR), and high-resolution mass spectrometry (HR-MS) analyses. Their biological potential was evaluated using *in vitro* assays, which included assessments of α-glucosidase inhibition, antibacterial activity, anti-inflammatory properties, and anticancer effects. Simultaneously, *in silico* studies involving molecular docking against chosen therapeutic targets, absorption, distribution, metabolism, excretion, and toxicity (ADMET) prediction, and molecular dynamics simulations were conducted to clarify binding behaviour and pharmacokinetic appropriateness. This combined experimental and computational method facilitates the identification of potential multi-target lead candidates.

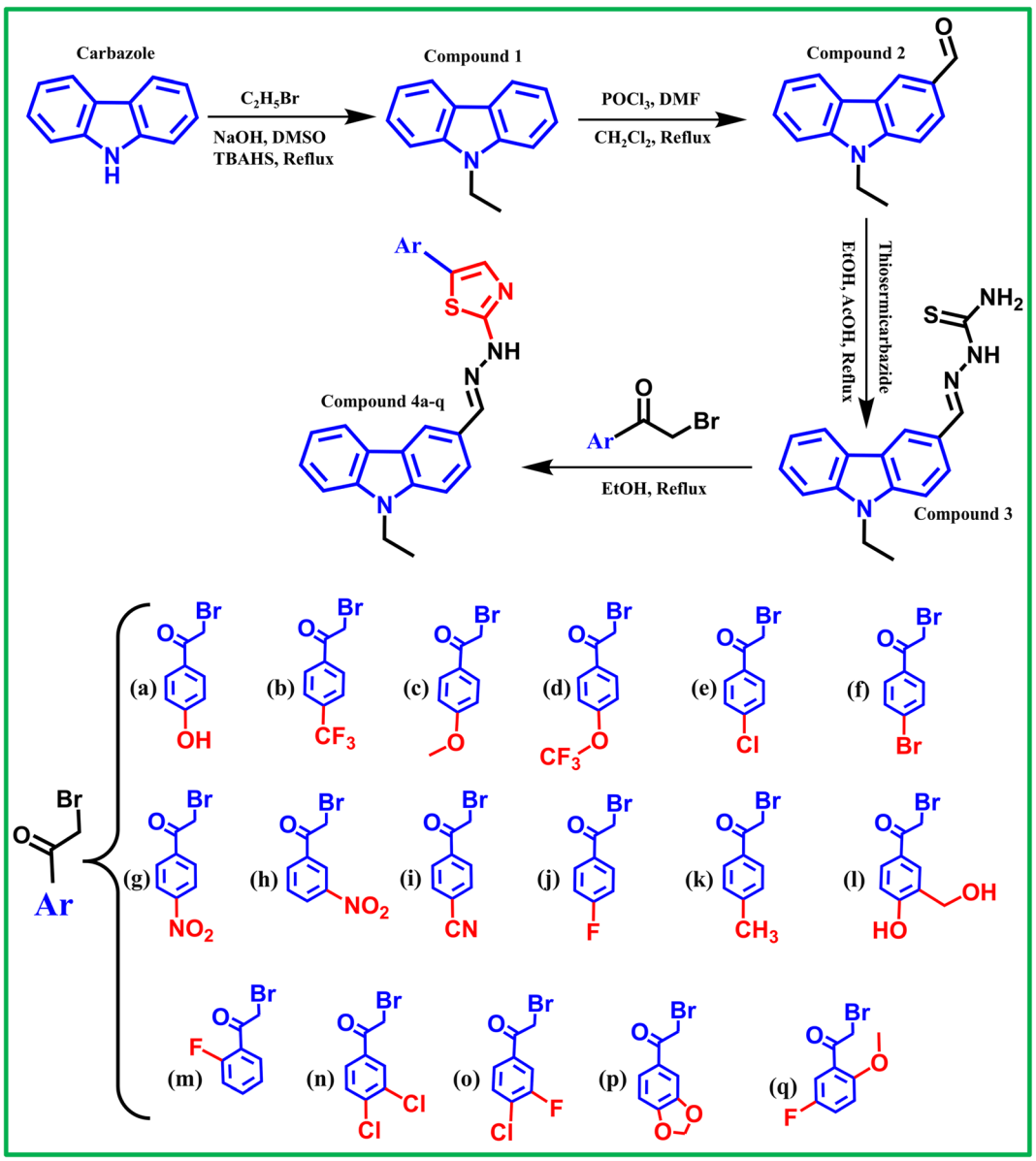

Scheme 1 Schematic representation of the synthetic pathway for 1,3-thiazole derivatives (4a–q).

2. Materials and methods

2.1. Materials

2.1.1. Chemical and apparatus. All reagents and solvents were of analytical grade and used without further purification. Compounds **4a–q** were synthesised according to the procedure described in Scheme 1. The reaction progress and purity of the products were monitored by thin-layer chromatography (TLC) on silica gel 60 F_{254} plates (Merck) using appropriate solvent systems and visualised under UV light (254/366 nm). Melting points were determined on a Stuart SMP50 apparatus and are uncorrected. FT-IR spectra were recorded on a PerkinElmer Spectrum 100 spectrometer using KBr discs. ^{1}H-NMR and ^{13}C-NMR spectra were acquired on a Bruker Avance 500 MHz spectrometer in deuterated dimethyl sulfoxide (DMSO-d_6) with tetramethylsilane (TMS) as the internal reference. High-resolution mass spectra were obtained using a Waters SYNAPT G2-S Q-TOF mass spectrometer.

2.1.2. Cell lines and cell culture. Human breast cancer cells (MCF-7), human lung carcinoma cells (A549), and human hepatocellular carcinoma cells (HepG2) were obtained from the American Type Culture Collection (ATCC, Manassas, USA). The murine macrophage cell line RAW 264.7, commonly used for anti-inflammatory studies, was also purchased from ATCC. Cells were cultured in Dulbecco's modified eagle medium (DMEM, Gibco) supplemented with 10% (v/v) foetal bovine serum (FBS, Sigma), 1% penicillin–streptomycin (100 IU ml^{-1} and 100 μg ml^{-1}, respectively), and 2 mM L-glutamine (Sigma). All cell lines were maintained at 37 °C in a humidified atmosphere containing 5% CO_2. Cells used in the experiments were between passages 4 and 20.[30]

2.1.3. Bacterial and fungal strains and culture conditions. The bacterial strains *Escherichia coli* ATCC 8739 (*E. coli*), *Staphylococcus aureus* ATCC 6538 (*S. aureus*), and *Salmonella typhimurium* ATCC 14028 (*S. typhimurium*), together with the fungal strain *Candida albicans* ATCC 10231 (*C. albicans*), were used in this study. All strains were obtained from the American Type Culture Collection (ATCC, Manassas, USA). Microorganisms were maintained and subcultured on nutrient agar or Sabouraud dextrose agar (for *C. albicans*) at 37 °C prior to use in antimicrobial assays.[31] The clinical isolates were obtained in 2024 from the Faculty of Biology and Biotechnology, University of Science, Vietnam National University.

2.2. Methods

2.2.1. Synthesis of compounds 1–3 and thiazole derivatives (4a–q). The synthesis of 1,3-thiazole derivatives (**4a–q**) was accomplished through four consecutive steps. As seen in Scheme 1, first, *N*-ethylcarbazole (**1**) was obtained by reacting carbazole (10 g, 0.06 mol) with ethyl bromide (6.7 mL, 0.09 mol) in DMSO (180 mL) using KOH (8.3750 g) and tetrabutylammonium hydrogen sulfate (TBAHS) (1.0153 g) as catalysts at 60–70 °C for 20 h. The mixture was quenched with water, and the precipitate was filtered and dried. In the second step, compound (**1**) (10.0 g, 0.051 mol) underwent Vilsmeier–Haack formylation with $POCl_3$/DMF to afford 9-ethyl-9*H*-carbazole-3-carbaldehyde (compound **2**), which was purified by recrystallization from *n*-hexane. Compound (**2**) (5.0 g, 0.022 mol) was then condensed with thiosemicarbazide (2.1905 g, 0.024 mol) in ethanol, using glacial acetic acid (0.1 mL) as a catalyst, at 60–70 °C for 6 h to yield the thiosemicarbazone (**3**). Finally, compound (**3**) (0.2 g) reacted with various α-bromoketones ($n_{\text{compound 3}} : n_{\text{bromoketone}} = 1:1$) in ethanol at 60–70 °C for 6 h under reflux to form the target 1,3-thiazole derivatives (**4a–4q**), which were purified by filtration, washed with ethanol, and confirmed for purity by TLC prior to structural characterization.[32]

2.2.2. Reaction mechanism. The proposed cyclocondensation mechanism is summarized in Scheme 2. Compound (**3**), a thiosemicarbazone derivative, reacts with α-bromo ketones in ethanol under reflux to afford the target 1,3-thiazole derivatives. The transformation proceeds through an initial nucleophilic substitution, in which the sulfur atom of the thioamide group attacks the α-carbon of the α-bromo ketone to generate a thioalkyl intermediate. An intramolecular nucleophilic addition of the adjacent amino nitrogen to the carbonyl carbon then induces ring closure to form the thiazole nucleus. Finally, elimination of HBr drives the reaction to completion, yielding the 2-substituted thiazole products.[33]

2.2.3. Physicochemistry of compounds

*2.2.3.1 Compound **1** (9-ethyl-9H-carbazole).* Colorless amorphous powder (10.9805 g), yield of 93.75%. ^{1}H-NMR (500 MHz, DMSO-d_6, 25 °C, δ ppm): 1.27 (t, J = 6.0 Hz, 3H, –C**H**$_2$–CH$_3$); 4.38–4.40 (m, 2H, –C**H**$_2$–CH$_3$); 7.20 (t, J = 6.0 Hz, 2H, aromatic–H (H-2; H-7)); 7.45 (t, J = 6.0 Hz, 2H, Ar–H (H-3, H-6)); 7.56 (d, J = 6.5 Hz, 2H, Ar–H (H-1, H-8)); 8.14 (d, J = 6.0 Hz, 2H, Ar–H (H-4, H-5)). ^{13}C-NMR (125 MHz, DMSO-d_6, 25 °C, δ ppm) 139.5; 125.6; 122.1; 120.2; 118.9; 108.9; 36.8 (–**C**H$_2$–CH$_3$); 13.5 (–CH$_2$–**C**H$_3$). Observation on the ^{1}H-NMR spectrum showed the appearance of a triplet signal at δ = 1.286 ppm corresponding to three

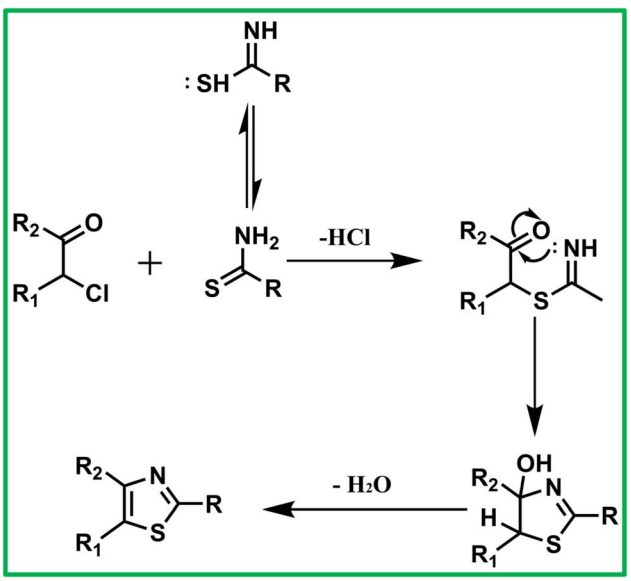

Scheme 2 Mechanistic representation of the Hantzsch-type process involved in constructing 1,3-thiazole ring.

protons and a multiplet signal at δ = 4.38–4.40 ppm corresponding to two protons.[32] In the ^{13}C-NMR spectrum, two signals were observed at δ = 36.8 and 13.5 ppm (Fig. S1–S4). These NMR signals confirm the presence of a –CH_2–CH_3 group attached to the carbazole framework.

*2.2.3.2 Compound **2** (9-ethyl-9H-carbazole-3-carbaldehyde).* Colorless amorphous powder (6.0612 g), yield of 51.14%. ^{1}H-NMR (500 MHz, DMSO-d_6, 25 °C, δ ppm): 1.32 (t, J = 6.0 Hz, 3H, –CH_2–C**H**$_3$); 4.52 (q, J = 6.0 Hz, 2H, –C**H**$_2$–CH_3); 7.32 (t, J = 6.0 Hz, 1H, Ar–H); 7.55 (t, J = 5.8 Hz, 1H, Ar–H); 7.79 (d, J = 7.0 Hz, 1H, Ar–H); 8.01 (dd, J_1 = 6.0 Hz, J_2 = 1.5 Hz, 1H, Ar–H); 8.76 (d, J = 1 Hz, 1H, Ar–H); 10.07 (s, 1H, –CHO). ^{13}C-NMR (125 MHz, DMSO-d_6, 25 °C, δ ppm) 191.8 (–CHO); 143.3; 140.0; 128.7; 126.7; 126.6; 123.9; 122.3; 122.2; 120.8; 120.1; 109.8; 109.5; 37.3 (–**C**H$_2$–CH_3); 13.6 (–CH_2–**C**H$_3$).[34] Observation of the ^{1}H-NMR spectrum, in addition to the characteristic signals of the ethyl group at δ = 1.35 ppm (t, J = 6.0 Hz, 3H, –CH_2–C**H**$_3$) and δ = 4.52 ppm (q, J = 6.0 Hz, 2H, –C**H**$_2$–CH_3), reveals the appearance of a singlet corresponding to one proton of the –CHO group at δ = 10.07 ppm (Fig. S5).[32] Similarly, the ^{13}C-NMR spectrum exhibits a signal at δ = 191.8 ppm, characteristic of the –CHO carbon. These results confirm the successful introduction of the carbonyl group at the C3 position of 9-ethyl-9*H*-carbazole, resulting in the formation of compound (**2**), 9-ethyl-9*H*-carbazole-3-carbaldehyde.

*2.2.3.3 Compound **3** (((9-ethyl-9H-carbazol-3-yl)methylene) hydrazine-1-carbothioamide).* Light yellow powder (6.0133 g), yield of 92.34%. ^{1}H-NMR (500 MHz, DMSO-d_6, 25 °C, δ ppm): 1.33 (t, J = 6.0 Hz, 3H, –CH_2–C**H**$_3$); 4.46 (q, J = 6.0 Hz, 2H, –C**H**$_2$–CH_3); 7.24 (t, J = 6.0 Hz, 1H, Ar–H); 7.48 (t, J = 6.0 Hz, 1H, Ar–H); 7.63 (d, J = 7.0 Hz, 3H, Ar–H, –NH_2); 7.97 (dd, J_1 = 6.0 Hz, J_2 = 1.5 Hz, 1H, Ar–H); 8.14 (s, 1H); 8.21 (d, J = 6.5 Hz, 1H); 8.23 (s, 1H, –CH=N–); 8.58 (d, J = 1.0 Hz, 1H, Ar–H); 11.36 (s, 1H, =N–NH–).[32]

^{13}C-NMR (125 MHz, DMSO-d_6, 25 °C, δ ppm) 177.5 (C=S); 143.6 (Ar–CH=N); 140.5; 140.0; 126.1; 125.1; 122.2; 120.6; 120.2; 119.2; 109.4; 37.1 (–**C**H$_2$–CH_3); 13.7 (–CH_2–**C**H$_3$).[32] The formation of the thiosemicarbazone group (Fig. S6–S9) was confirmed by the disappearance of the –CHO proton signal (δ = 10.07 ppm) and the appearance of a new singlet signal at δ = 11.36 ppm corresponding to the =N–NH– proton, as well as another singlet at δ = 8.23 ppm assigned to the –CH=N– group in the ^{1}H-NMR spectrum.[32] Similarly, in the ^{13}C-NMR spectrum, signals at δ = 177.5 (C=S) and 143.6 (Ar–CH=N–) were observed. These results confirmed the successful formation of compound (**3**) (((9-ethyl-9*H*-carbazol-3-yl)methylene)hydrazine-1-carbothioamide) with no detectable impurities.

The physicochemical properties of compounds **4a–q** (Fig. S10–S81) are as follows:

*2.2.3.4 4-(2-(2-((9-Ethyl-9H-carbazol-3-yl)methylene) hydrazone)thiazol-4-yl)phenol (**4a**).* Chemical formula: $C_{24}H_{20}N_4OS$; colorless amorphous powder (0.1743 g); yield of 62.63%; melting point: 277–278 °C; R_f = 0.27 (V_{hexane} : $V_{ethyl\ acetate}$ = 7 : 3); IR (λ_{max}, cm^{-1}, KBr): 3238 (–OH, –CH stretching vibration); 3076 (–CH_3); 2988 (–CH_2–); 2934, 2888 (CH aromatic); 1615 (C=N azomethine, C=N thiazole); 1231 (Ar–O–); 1091 (=N–NH–); 830, 743 (aromatic ring bearing substituents). ^{1}H-NMR (500 MHz, DMSO-d_6, 25 °C) δ (ppm): 1.33 (t, J = 6.0 Hz, 3H, –CH_2–C**H**$_3$); 4.46 (q, J = 6.0 Hz, 3H, –C**H**$_2$–CH_3; R–O**H**); 6.84 (d, J = 7.5 Hz, 2H); 7.08 (s, 1H, H–C5-thiazole); 7.25 (t, J = 6.0 Hz, 1H), 7.49 (t, J = 6.3 Hz 1H), 7.63–7.69 (m, 4H), 7.89 (d, J = 7.5 Hz, 1H), 8.21 (d, J = 6.5 Hz, 1H); 8.34 (s, 1H); 8.41 (s, 1H). ^{13}C-NMR (125 MHz, DMSO-d_6, 25 °C) δ (ppm): 168.2 (quaternary carbon, C2-thiazole); 157.2 (quaternary carbon, C–OH); 140.2 (–CH=N–); 139.9 (quaternary carbon, C9a-carbazole); 127.0, 126.1 (quaternary carbon, C4a, 8a-carbazole); 125.3 (quaternary carbon, C4-phenyl, C4b-carbazole); 123.6 (quaternary carbon, C3-carbazole); 122.3; 122.1; 120.6; 119.7; 119.3; 115.3; 109.7; 109.4; 100.3 (C5-thiazole); 37.1 (–**C**H$_2$–CH_3); 13.7 (–CH_2–**C**H$_3$). HR-MS (ESI$^+$): m/z [M + H]$^+$ calcd for $C_{24}H_{20}N_4OS$: 413.1436, found: 413.1434.

*2.2.3.5 2-(2-((9-Ethyl-9H-carbazol-3-yl)methylene)hydrazone)-4-(4-(trifluoromethyl)phenyl)thiazole (**4b**).* Chemical formula: $C_{25}H_{19}F_3N_4S$; light brown powder (0.1744 g), yield of 55.64%; melting point: 177–178 °C; R_f = 0.27 (V_{hexane} : $V_{ethyl\ acetate}$ = 7 : 3); IR (λ_{max}, cm^{-1}, KBr): 3357 (–CH stretching vibration); 3072 (–CH_3); 2934, 2891 (–CH_2–); 1629 (C=N azomethine, C=N thiazole); 1481, 1568 (C=C aromatic); 1324, 1115 (–CF_3); 1066 (=N–NH–); 844, 748 (aromatic ring bearing substituents). ^{1}H-NMR (500 MHz, DMSO-d_6, 25 °C) δ (ppm): 1.34 (t, J = 6.0 Hz, 3H, –CH_2–C**H**$_3$); 4.47 (q, J = 6.0 Hz, 2H, –C**H**$_2$–CH_3); 7.24 (t, J = 6.0 Hz, 1H); 7.49 (t, J = 6.5 Hz,1H); 7.56 (s, 1H, (H–C5-thiazole)); 7.64 (d, J = 6.5 Hz, 1H); 7.68 (d, J = 7.5 Hz, 1H); 7.77 (d, J = 7.0 Hz, 2H); 7.87 (d, J = 7.0 Hz, 1H); 8.08 (d, J = 7.0 Hz, 2H, –CH=N–; H–C1-carbazole); 8.22 (d, J = 6.5 Hz, 1H); 8.24 (s, 1H); 8.38 (s, 1H); 12.10 (s, 1H, =N–NH–). ^{13}C-NMR (125 MHz, DMSO-d_6, 25 °C) δ (ppm): 168.7 (quaternary carbon, C2-thiazole); 148.9 (quaternary carbon, C4-thiazole); 143.1 (–CH=N–); 140.2 (quaternary carbon, C9a-carbazole); 139.9 (quaternary carbon, C1-phenyl); 138.4 (quaternary carbon, C4-phenyl); 127.6; 127.3; 126.1 (quaternary carbon, C4a, 8a-carbazole); 126.0; 125.5; 125.5; 125.3; 125.2 (quaternary carbon, C4b-carbazole); 123.5 (quaternary carbon, C3-carbazole); 123.4 (quaternary carbon, –**C**F_3); 122.3; 122.1; 120.5; 119.6; 119.2; 109.6; 109.4; 106.0 (C5-thiazole); 37.1 (–**C**H$_2$–CH_3); 13.7 (–CH_2–**C**H$_3$). HR-MS (ESI$^+$): m/z [M + H]$^+$ calcd for $C_{25}H_{19}F_3N_4S$: 465.1361, found: 465.1357.

*2.2.3.6 2-(2-((9-Ethyl-9H-carbazol-3-yl)methylene)hydrazone)-4-(4-methoxyphenyl)thiazole (**4c**).* Chemical formula: $C_{25}H_{22}N_4OS$; light orange powder (0.2802 g); yield of 97.29%; melting point: 267–268 °C; R_f = 0.26 (V_{hexane} : $V_{ethyl\ acetate}$ = 8 : 2); IR (λ_{max}, cm^{-1}, KBr): 3349 (–CH stretching vibration); 3013 (–CH_3); 2961 (–CH_2–); 2765 (–O–CH_3); 1620 (C=N azomethine, C=N thiazole); 1508, 1471 (C=C aromatic); 1239, 1184, 1025 (Ar–O–CH_3); 821, 750 (aromatic ring bearing substituents).^{1}H-NMR (500 MHz, DMSO-d_6, 25 °C) δ (ppm): 1.34 (t, J = 6.0 Hz, 3H, –CH_2–C**H**$_3$); 3.80 (s, 3H, –O–CH_3); 4.47 (t, J = 6.0 Hz, 2H, –C**H**$_2$–CH_3); 6.98–7.00 (m, 2H), 7.15 (s, 1H, H–C5-thiazole); 7.25 (t, J = 6.3 Hz, 1H); 7.49 (t, J = 6.5, 1H); 7.64 (d, J = 7.0 Hz, 1H); 7.69 (d, J = 7.0 Hz, 1H); 7.78–7.81 (m, 2H); 7.87 (dd, J_1 = 7.3 Hz, J_2 = 1.3 Hz, 1H); 8.22 (d, J = 6.5 Hz, 1H); 8.25 (s, 1H); 8.39 (s, 1H). ^{13}C-NMR (125 MHz, DMSO-d_6, 25 °C) δ (ppm): 168.3 (quaternary carbon, C2-thiazole); 158.9 (quaternary carbon, C4-phenyl); 143.5 (quaternary carbon, C4-thiazole); 140.3 (–CH=N–); 140.0 (quaternary carbon, C9a-carbazole), 127.0;

126.2 (quaternary carbon, C4a, 8a-carbazole); 125.3 (quaternary carbon, C4b-carbazole; C1-phenyl); 123.6 (quaternary carbon, C3-carbazole); 122.3; 122.1; 120.6; 119.7; 119.3; 114.0; 109.7; 109.4; 101.2 (C5-thiazole); 55.2 (–O–CH_3); 37.2 (–**C**H_2–CH_3); 13.7 (–CH_2–**C**H_3). HR-MS (ESI^+): m/z $[M + H]^+$ calcd for $C_{25}H_{22}N_4OS$: 427.1592, found: 427.1595.

*2.2.3.7 2-(2-((9-Ethyl-9H-carbazol-3-yl)methylene)hydrazone)-4-(4-(trifluoromethoxy)phenyl)thiazole (**4d**).* Chemical formula: $C_{25}H_{19}F_3N_4OS$; white orange powder (0.2731 g); yield of 84.19%; melting point: 253–254 °C; $R_f = 0.66$ ($V_{Hexane} : V_{Ethyl\ acetate} = 8:2$); IR ($\lambda_{max}$, cm^{-1}, KBr): 3079 (–CH_3); 2977, 2938 (–CH_2–); 1626 (CH=N azomethine, C=N thiazole); 1598, 1564, 1491 (C=C aromatic); 1263, 1229, 1162 (Ar–O–CF_3); 1046, 1017 (=N–NH–); 848, 737 (aromatic ring bearing substituents).^{1}H-NMR (500 MHz, DMSO-d_6, 25 °C) δ (ppm): 1.34 (t, $J = 6.0$ Hz, 3H, –CH_2–C**H**$_3$); 4.47 (q, $J = 6.0$ Hz, 2H, –C**H**$_2$–CH_3); 7.25 (t, $J = 6.0$ Hz, 1H); 7.41 (s, 2H); 7.42 (s, 1H, H–C5-thiazole); 7.49 (t, $J = 6.3$ Hz, 1H); 7.64 (d, $J = 7.0$ Hz, 1H); 7.69 (d, $J = 6.0$ Hz, 1H); 7.87 (dd, $J_1 = 7.0$ Hz, $J_2 = 1.0$ Hz, 1H); 7.97–8.00 (m, 2H, –CH=N–; H–C1-carbazole); 8.22 (s, 1H); 8.23 (s,1H); 8.38 (d, $J = 6.5$ Hz, 1H). ^{13}C-NMR (125 MHz, DMSO-d_6, 25 °C) δ (ppm): 168.6 (quaternary carbon, C2-thiazole); 148.9 (quaternary carbon, C4-thiazole); 143.1 (–CH=N–); 140.2 (quaternary carbon, C9a-carbazole); 139.9; 133.9 (quaternary carbon, R–CF_3); 127.3, 126.1 (quaternary carbon, C4a, 8a-carbazole); 125.3 (quaternary carbon, C4b-carbazole; C1-phenyl); 123.5 (quaternary carbon, C3-carbazole); 122.3; 122.1; 121.1; 120.5; 119.6; 119.2; 109.6; 109.4; 104.3 (C5-thiazole); 37.1 (–**C**H_2–CH_3); 13.7 (–CH_2–**C**H_3). HR-MS (ESI^+): m/z $[M + H]^+$ calcd for $C_{25}H_{19}N_4OSF_3$: 481.1310, found: 481.1308.

*2.2.3.8 4-(4-Chlorophenyl)-2-(2-((9-ethyl-9H-carbazol-3-yl) methylene)hydrazone)thiazole (**4e**).* Chemical formula: $C_{24}H_{19}ClN_4S$; white orange powder (0.2783 g); yield of 85.47%; melting point: 259–260 °C; $R_f = 0.56$ ($V_{hexane} : V_{ethyl\ acetate} = 8:2$); IR ($\lambda_{max}$, cm^{-1}, KBr): 3294 (–CH stretching vibration); 3091, 3021 (–CH_3–); 2971, 2932 (–CH_2–); 1606 (C=N azomethine, C=N thiazole); 1481 (C=C aromatic); 1044, 1013 (=N–NH–); 820, 740 (aromatic ring bearing substituents); 616, 551 (Ar–Cl).^{1}H-NMR (500 MHz, DMSO-d_6, 25 °C) δ (ppm): 1.33 (t, $J = 6.0$ Hz, 3H, –CH_2–C**H**$_3$); 4.46 (q, $J = 6.0$ Hz, 2H, –C**H**$_2$–CH_3); 7.24 (t, $J = 6.0$ Hz, 1H); 7.39 (s, 1H, H–C5-thiazole); 7.46–7.50 (m, 3H); 7.63 (d, $J = 7.0$ Hz, 1H); 7.68 (d, $J = 7.5$ Hz, 1H); 7.85–7.89 (m, 3H); 8.22 (d, $J = 6.5$ Hz, 1H); 8.24 (s, 1H); 8.38 (s, 1H). ^{13}C-NMR (125 MHz, DMSO-d_6, 25 °C) δ (ppm): 168.5 (quaternary carbon, C2-thiazole); 149.0 (quaternary carbon, C4-thiazole); 143.2 (–CH=N–); 140.2 (quaternary carbon, C9a-carbazole); 139.9; 133.5 (quaternary carbon, C4-phenyl); 131.9 (quaternary carbon, C1-phenyl); 128.6; 127.2; 126.1 (quaternary carbon, C4a, 8a-carbazole); 125.3 (quaternary carbon, C4b-carbazole); 123.6; (quaternary carbon, C3-carbazole); 122.3; 122.1; 120.6; 119.6; 119.2; 109.7; 109.4; 104.1 (C5-thiazole); 37.1 (–**C**H_2–CH_3); 13.7 (–CH_2–**C**H_3). HR-MS (ESI^+): m/z $[M + H]^+$ calcd for $C_{24}H_{19}N_4SCl$: 431.1091, found: 431.1091.

*2.2.3.9 4-(4-Bromophenyl)-2-(2-((9-ethyl-9H-carbazol-3-yl) methylene)hydrazone)thiazole (**4f**).* Chemical formula: $C_{24}H_{19}BrN_4S$; white orange powder (0.2911 g); yield of 90.89%; melting point: 259–260 °C; $R_f = 0.54$ ($V_{hexane} : V_{ethyl\ acetate} = 8:2$); IR($\lambda_{max}$, cm^{-1}, KBr): 3298 (–CH stretching vibration); 3094 (–CH_3); 2969 (–CH_2–); 1622 (C=N azomethine, C=N thiazole); 1483 (C=C aromatic); 1233, 1192 (C–N); 1043, 1009 (=N–NH–); 819, 740 (aromatic ring bearing substituents); 617, 520 (Ar–Br).^{1}H-NMR (500 MHz, DMSO-d_6 25 °C) δ (ppm): 1.34 (t, $J = 6.0$ Hz, 3H, –CH_2–C**H**$_3$); 4.46 (q, $J = 6.0$ Hz, 2H, –C**H**$_2$–CH_3); 7.25 (t, $J = 6.0$ Hz, 1H); 7.40 (s, 1H, H–C5-thiazole); 7.49 (t, $J = 6.5$ Hz, 1H); 7.60–7.65 (m, 3H); 7.68 (d, $J = 7.0$ Hz, 1H); 7.81–7.83 (m, 2H); 7.87 (dd, $J_1 = 7.3$ Hz, $J_2 = 1.3$ Hz, 1H); 8.22 (d, $J = 6.5$ Hz, 1H); 8.25 (s, 1H); 8.39 (s, 1H). ^{13}C-NMR (125 MHz, DMSO-d_6, 25 °C) δ (ppm): 168.6 (quaternary carbon, C2-thiazole); 149.0 (quaternary carbon, C4-thiazole); 143.2 (–CH=N–); 140.2 (quaternary carbon, C9a-carbazole); 140.0; 133.8; 131.5 (quaternary carbon, C1-phenyl); 127.6, 126.1 (quaternary carbon, C4a, 8a-carbazole); 125.4 (quaternary carbon, C3-carbazole); 123.6 (quaternary carbon, C4b-carbazole); 122.3 (quaternary carbon, C4-phenyl); 122.3; 120.6; 120.5; 119.6; 119.3; 109.7; 109.4; 104.2 (C5-thiazole); 37.1 (–**C**H_2–CH_3); 13.7 (–CH_2–**C**H_3). HR-MS (ESI^+): m/z $[M + H]^+$ calcd for $C_{24}H_{19}N_4SBr$: 475.0592, found: 475.0588.

*2.2.3.10 2-(2-((9-Ethyl-9H-carbazol-3-yl)methylene) hydrazone)-4-(4-nitrophenyl)thiazole (**4g**).* Chemical formula: $C_{24}H_{19}N_5O_2S$; orange powder (0.2441 g); yield of 81.92%; melting point: 264–265 °C; $R_f = 0.72$ ($V_{hexane} : V_{ethyl\ acetate} = 7:3$); IR ($\lambda_{max}$, cm^{-1}, KBr): 3313 (–CH stretching vibration); 3058 (–CH_3–); 2976, 2928 (–CH_2–); 1584 (C=N azomethine, C=N thiazole); 1501, 1336, 1235 (–NO_2); 1476 (C=C aromatic); 1050 (=N–NH–); 854, 748 (aromatic ring bearing substituents).^{1}H NMR (500 MHz, DMSO-d_6, 25 °C) δ (ppm): 1.34 (t, $J = 6.0$ Hz, 3H, –CH_2–C**H**$_3$); 4.47 (q, $J = 6.0$ Hz, 2H, –C**H**$_2$–CH_3); 7.25 (t, $J = 6.3$ Hz, 1H); 7.49 (t, $J = 6.3$ Hz, 1H); 7.64 (d, $J = 7.0$ Hz, 1H); 7.68 (d, $J = 7.0$ Hz, 1H); 7.71 (s, 1H); 7.87 (dd, $J_1 = 7.0$ Hz, $J_2 = 1.0$ Hz, 1H); 8.13 (d, $J = 7.5$ Hz, 2H); 8.22 (d, $J = 6.5$ Hz, 1H); 8.24 (s, 1H); 8.28 (d, $J = 7.0$ Hz, 2H); 8.38 (s, 1H); 12.15 (s, 1H, =N–NH–). ^{13}C-NMR (125 MHz, DMSO-d_6, 25 °C) δ (ppm): 168.8 (quaternary carbon, C2-thiazole); 148.5 (quaternary carbon, C4-thiazole); 143.3 (–CH=N–); 140.8 (quaternary carbon, C9a-carbazole); 140.2 (quaternary carbon, C4-phenyl); 139.9 (quaternary carbon, C1-phenyl); 126.3 (quaternary carbon, C4a, 8a-carbazole); 126.1 (quaternary carbon, C1-carbazole); 125.3; 124.1 (quaternary carbon, C3-carbazole); 123.6; 122.3; 122.1; 120.6; 119.7; 119.2; 109.7; 109.4; 108.1 (C5-thiazole); 37.1 (–**C**H_2–CH_3); 13.7 (–CH_2–**C**H_3). HR-MS (ESI^+): m/z $[M + H]^+$ calcd for $C_{24}H_{19}N_5SO_2$: 442.1337, found: 442.1332.

*2.2.3.11 2-(2-((9-Ethyl-9H-carbazol-3-yl)methylene) hydrazone)-4-(3-nitrophenyl)thiazole (**4h**).* Chemical formula: $C_{24}H_{19}N_5O_2S$; light gray black powder (0.1945 g); yield of 65.29%; melting point: 268–269 °C; $R_f = 0.34$ ($V_{hexane} : V_{ethyl\ acetate} = 7:3$); IR ($\lambda_{max}$, cm^{-1}, KBr): 3239 (–CH stretching vibration); 3064 (–CH_3–); 2983, 2880 (–CH_2–); 1630 (C=N azomethine, C=N thiazole); 1531, 1346 (–NO_2); 1596, 1486 (C=C aromatic); 1088 (=N–NH–); 890, 737 (aromatic ring bearing substituents). ^{1}H-NMR (500 MHz, DMSO-d_6, 25 °C) δ (ppm): 1.34 (t, $J = 6.0$ Hz, 3H, –CH_2–C**H**$_3$); 4.48 (q, $J = 6.0$ Hz, 2H, –C**H**$_2$–CH_3); 7.25 (t, $J = 6.0$ Hz, 1H); 7.49 (t, $J = 6.4$ Hz, 1H); 7.64–7.66 (m, 2H); 7.69 (d, $J = 7.0$ Hz, 1H); 7.72 (t, $J = 6.8$ Hz, 1H); 7.87 (dd, $J_1 = 7.3$ Hz, $J_2 = 1.5$ Hz, 1H); 8.15–8.17 (m, 1H); 8.22–8.24 (m, 2H); 8.32 (d, $J = 6.5$ Hz, 1H); 8.39 (s, 1H); 8.70 (t, $J = 1.8$ Hz, 1H); 12.18 (s, 1H, =

N–NH–). ^{13}C-NMR (125 MHz, DMSO-d$_6$, 25 °C) δ (ppm): 168.8 (quaternary carbon, C2-thiazole); 148.3 (quaternary carbon, C4-thiazole); 148.0 (quaternary carbon, C3-phenyl); 143.3 (–CH=N–); 140.3 (quaternary carbon, C9a-carbazole); 140.0; 136.2 (quaternary carbon, C1-phenyl); 131.6; 130.2, 126.2 (quaternary carbon, C4a, 8a-carbazole); 125.3 (quaternary carbon, C4b-carbazole); 123.6 (quaternary carbon, C3-carbazole); 122.3; 122.1; 120.6; 119.9; 119.7; 119.3; 109.7; 109.4; 106.0 (C5-thiazole); 37.2 (–**C**H$_2$–CH$_3$); 13.7 (–CH$_2$–**C**H$_3$). HR-MS (ESI$^+$): m/z [M + H]$^+$ calcd for $C_{24}H_{19}N_5SO_2$: 442.1337, found: 442.1341.

*2.2.3.12 4-(2-(2-((9-Ethyl-9H-carbazol-3-yl)methylene) hydrazone)thiazol-4-yl)benzonitrile (**4i**).* Chemical formula: $C_{25}H_{19}N_5S$; light orange powder (0.2746 g); yield of 96.54%; melting point: 273–274 °C; $R_f = 0.50$ ($V_{hexane} : V_{ethyl\ acetate} = 7:3$); IR ($\lambda_{max}$, cm^{-1}, KBr): 3242 (–CH stretching vibration); 3123, 3054 (–CH$_3$); 2986 (–CH$_2$–); 2888 (CH aromatic); 2224 (–C≡N); 1616 (C=N azomethine, C=N thiazole); 1489 (C=C aromatic); 1385, 1337 (C–S); 1235, 1193 (C–N); 1087, 1033 (=N–NH–); 839, 749 (aromatic ring bearing substituents). ^{1}H-NMR (500 MHz, DMSO-d$_6$, 25 °C) δ (ppm): 1.34 (t, $J = 5.8$ Hz, 3H, –CH$_2$–C**H**$_3$); 4.47 (q, $J = 5.3$ Hz, 2H, –C**H**$_2$–CH$_3$); 7.24 (t, $J = 6.0$ Hz, 1H); 7.49 (t, $J = 6.5$ Hz, 1H); 7.63–7.65 (m, 2H); 7.68 (dd, $J_1 = 7.0$ Hz, $J_2 = 1.5$ Hz, 1H); 7.86–7.88 (m, 3H, Ar–H); 8.04–8.06 (m, 2H, Ar–H); 8.22 (d, $J = 6.5$ Hz, 1H, Ar–H); 8.25 (s, 1H); 8.38 (s, 1H); 12.11 (s, 1H, =N–NH–). ^{13}C-NMR (125 MHz, DMSO-d$_6$, 25 °C) δ (ppm): 168.7 (quaternary carbon, C2-thiazole); 148.7 (quaternary carbon, C4-thiazole); 143.3 (–CH=N–); 140.2 (quaternary carbon, C9a-carbazole); 139.95; 138.8 (quaternary carbon, C4-phenyl); 132.6, 126.1 (quaternary carbon, C4a, 8b-carbazole), 125.3 (quaternary carbon, C4b-carbazole); 123.6 (quaternary carbon, C3-carbazole); 122.3; 122.1; 120.6; 119.7; 119.3; 119.0 (quaternary carbon, –C≡N); 109.7 (quaternary carbon, C1-phenyl); 109.5; 107.1 (C5-thiazole); 37.1 (–**C**H$_2$–CH$_3$); 13.7 (–CH$_2$–**C**H$_3$). HR-MS (ESI$^+$): m/z [M + H]$^+$ calcd for $C_{25}H_{19}N_5S$: 422.1439, found: 422.1445.

*2.2.3.13 2-(2-((9-Ethyl-9H-carbazol-3-yl)methylene) hydrazone)-4-(4-fluorophenyl)thiazole (**4j**).* Chemical formula: $C_{24}H_{19}FN_4S$; pale yellow powder (0.1908 g); yield of 68.22%; melting point: 257–258 °C; $R_f = 0.75$ ($V_{hexane} : V_{ethyl\ acetate} = 7:3$); IR ($\lambda_{max}$, cm^{-1}, KBr): 3234 (–CH stretching vibration); 3059 (–CH$_3$); 2976, 2932 (–CH$_2$–); 1615 (C=N azomethine, C=N thiazole); 1494 (C=C aromatic); 1234 (C–N aromatic, Ar–F); 1131 (Ar–F); 1086, 1044 (=N–NH–); 837, 748 (aromatic ring bearing substituents). ^{1}H-NMR (500 MHz, DMSO-d$_6$, 25 °C) δ (ppm): 1.34 (t, $J = 6.0$ Hz, 3H, –CH$_2$–C**H**$_3$); 4.47 (q, $J = 6.0$ Hz, 2H, –C**H**$_2$–CH$_3$); 7.23–7.26 (m, 3H); 7.29 (s, 1H, H–C5-thiazole); 7.49 (t, $J = 6.4$ Hz, 1H); 7.64 (d, $J = 6.5$ Hz, 1H); 7.68 (d, $J = 7.5$ Hz, 1H); 7.86 (dd, $J_1 = 7.0$ Hz, $J_2 = 1.5$ Hz, 1H); 7.89–7.92 (m, 2H (–CH=N– and H–C1-carbazole)); 8.21–8.23 (m, 2H); 8.37 (s, 1H); 12.05 (s, 1H, =N–NH–). ^{13}C-NMR (125 MHz, DMSO-d$_6$, 25 °C) δ (ppm): 168.5 (quaternary carbon, C2-thiazole); 160.7 (quaternary carbon, –CF$_3$); 143.0 (–CH=N–); 140.2 (quaternary carbon, C9a-carbazole); 139.9; 131.3; 127.5 (quaternary carbon, C1-phenyl); 126.1 (quaternary carbon, C4a, 8a-carbazole); 125.4 (quaternary carbon, C4b-carbazole); 123.5 (quaternary carbon, C3-carbazole); 122.3; 122.1; 120.5; 119.6; 119.2; 115.4; 115.3; 109.6; 109.4; 103.0 (C5-thiazole); 37.1 (–**C**H$_2$–CH$_3$); 13.7 (–CH$_2$–**C**H$_3$). HR-MS (ESI$^+$): m/z [M + H]$^+$ calcd for $C_{24}H_{19}N_4SF$: 415.1392, found: 415.1397.

*2.2.3.14 2-(2-((9-Ethyl-9H-carbazol-3-yl)methylene)hydrazone)-4-(p-tolyl)thiazole (**4k**).* Chemical formula: $C_{25}H_{22}N_4S$; brown powder (0.2101 g); yield of 75.85%; melting point: 279–280 °C; $R_f = 0.65$ ($V_{hexane} : V_{ethyl\ acetate} = 7:3$); IR ($\lambda_{max}$, cm^{-1}, KBr): 3240 (–CH stretching vibration); 3045 (–CH$_3$); 2976 (–CH$_2$–); 2756, 1491 (Ar-CH$_3$); 1617 (C=N azomethine, C=N thiazole); 1491 (C=C aromatic); 1233 (C–N); 1087, 1034 (=N–NH–); 814, 743 (aromatic ring bearing substituents). ^{1}H-NMR (500 MHz, DMSO-d$_6$, 25 °C) δ (ppm): 1.34 (t, $J = 6.0$ Hz, 3H, –CH$_2$–C**H**$_3$); 2.33 (s, 3H, phenyl–CH$_3$); 4.47 (q, $J = 6.0$ Hz, 2H, –C**H**$_2$–CH$_3$); 7.22–7.26 (m, 4H, H–C5-thiazole; H–C6-carbazole; H–C$_3$,C$_5$-tolyl); 7.48–7.50 (m, 1H); 7.64 (d, $J = 6.5$ Hz,1H); 7.68 (d, $J = 7.0$ Hz, 1H); 7.75 (d, $J = 7.0$ Hz, 2H); 7.87 (dd, $J_1 = 7.3$ Hz, $J_2 = 1.3$ Hz, 1H); 8.22 (d, $J = 6.5$ Hz, 2H); 8.24 (s, 1H); 8.38 (d, $J = 1.5$ Hz, 1H). ^{13}C-NMR (125 MHz, DMSO-d$_6$, 25 °C) δ (ppm): 168.3 (quaternary carbon, C2-thiazole); 143.1 (–CH=N–); 140.2 (quaternary carbon, C9a-carbazole); 140.0; 136.8 (quaternary carbon, C4-phenyl); 129.1 (quaternary carbon, C1-phenyl); 126.1 (quaternary carbon, C4a, 8a-carbazole); 125.5; 125.4 (quaternary carbon, C4b-carbazole); 123.6 (quaternary carbon, C3-carbazole); 122.3; 122.1; 120.6; 119.6; 119.2; 109.7; 109.4; 102.3 (C5-thiazole); 56.0; 37.1 (–**C**H$_2$–CH$_3$); 20.8 (–CH$_3$); 18.5; 13.7 (–CH$_2$–**C**H$_3$). HR-MS (ESI$^+$): m/z [M + H]$^+$ calcd for $C_{25}H_{22}N_4S$: 411.1643, found: 411.1651.

*2.2.3.15 4-(2-(2-((9-Ethyl-9H-carbazol-3-yl)methylene) hydrazone)thiazol-4-yl)-2-(hydroxymethyl)phenol (**4l**).* Chemical formula: $C_{25}H_{22}N_4O_2S$; stone brown powder (0.2432 g); yield of 81.45%; melting point: 280–281 °C; $R_f = 0.22$ ($V_{hexane} : V_{ethyl\ acetate} = 5:5$); IR ($\lambda_{max}$, cm^{-1}, KBr): 3417, 3309 (–OH, –CH stretching vibration); 3064 (-CH$_3$); 2978, 2905 (–CH$_2$–); 1610 (C=N azomethine, C=N thiazole); 1498 (C=C aromatic); 1388 (–CH$_2$–OH); 1268, 1233, 1205 (Ar–OH, C–N); 1092, 1031 (=N–NH–; –CH$_2$–OH); 876, 807, 738 (aromatic ring bearing substituents). ^{1}H-NMR (500 MHz, DMSO-d$_6$, 25 °C) δ (ppm): 1.33 (t, $J = 6.0$ Hz, 3H, –CH$_2$–C**H**$_3$); 4.47 (q, $J = 6.0$ Hz, 2H, –C**H**$_2$–CH$_3$); 4.53 (s, 2H, –C**H**$_2$OH); 6.82 (d, $J = 7.0$ Hz, 1H, H–C6-phenyl); 7.02 (s, 1H, –CH$_2$O**H**); 7.25 (t, $J = 6.1$ Hz, 1H); 7.50 (t, $J = 7.0$ Hz, 1H); 7.54 (dd, $J_1 = 7.0$ Hz, $J_2 = 2.0$ Hz, 1H); 7.64 (d, $J = 6.5$ Hz, 1H); 7.69 (d, $J = 7.0$ Hz, 1H); 7.83 (d, $J = 1.5$ Hz, 1H); 7.88 (d, $J = 6.5$ Hz, 1H); 8.22 (d, $J = 6.5$ Hz, 1H); 8.28 (s, 1H); 8.40 (s, 1H). ^{13}C-NMR (125 MHz, DMSO-d$_6$, 25 °C) δ (ppm): 168.1 (quaternary carbon, C2-thiazole); 154.2 (quaternary carbon, C1-phenyl); 140.3 (–CH=N–); 140.0 (quaternary carbon, C9a-carbazole); 128.7 (quaternary carbon, C2-phenyl); 126.2 (quaternary carbon, C4a, 8a-carbazole); 125.1 (quaternary carbon, C4b-carbazole); 124.9 (quaternary carbon, C4-phenyl); 123.7 (quaternary carbon, C3-carbazole); 122.3; 122.1; 120.6; 119.8; 119.3; 114.6; 109.7; 109.4; 100.3 (C5-thiazole); 58.2 (–CH$_2$–OH); 37.1 (–**C**H$_2$–CH$_3$); 13.7 (–CH$_2$–**C**H$_3$). HR-MS (ESI$^+$): m/z [M + H]$^+$ calcd for $C_{25}H_{22}N_4SO_2$: 443.1541, found: 443.1538.

In addition, tandem mass spectrometry (MS/MS) analysis was performed for compound **4l**. The MS/MS spectrum of the [M + H]$^+$ ion (m/z 443.1560) exhibited characteristic product ions at m/z = 223.1244, 167.0725, 196.1118, 203.0277, and

205.0438…, which are consistent with the proposed structure of compound **4l** (Fig. S106).

*2.2.3.16 2-(2-((9-Ethyl-9H-carbazol-3-yl)methylene) hydrazone)-4-(2-fluorophenyl)thiazole (**4m**).* Chemical formula: $C_{24}H_{19}FN_4S$; tortila powder (0.1967 g); yield of 70.33%; melting point: 242–243 °C; R_f = 0.67 (V_{hexane} : $V_{ethyl\ acetate}$ = 7 : 3); IR (λ_{max}, cm^{-1}, KBr): 3401 (–CH stretching vibration); 3059 (–CH_3); 2976 (–CH_2–); 1619 (C=N azomethine, C=N thiazole); 1486 (C=C aromatic); 1338, 1274, 1235, 1125, 1084, 1021 (Ar–F, C–N, =N–NH–); 872, 804, 752 (aromatic ring bearing substituents). ^{1}H-NMR (500 MHz, DMSO-d_6, 25 °C) δ (ppm): 1.33 (t, J = 6.0 Hz, 3H, –CH_2–C**H**$_3$); 4.47 (q, J = 6.0 Hz, 2H, –C**H**$_2$–CH_3); 7.23–7.25 (m, 2H, H–C5-thiazole; H–C5-phenyl); 7.28–7.31 (m, 2H); 7.35–7.39 (m, 1H); 7.47–7.50 (m, 1H); 7.64 (d, J = 7.0 Hz, 1H); 7.68 (d, J = 7.0 Hz, 1H); 7.87 (dd, J_1 = 6.5 Hz, J_2 = 1.5 Hz, 1H); 8.01–8.04 (m, 1H, –CH=N–); 8.22 (d, J = 6.5 Hz, 1H); 8.25 (s, 1H); 8.38 (d, J = 1.0 Hz, 1H). ^{13}C-NMR (125 MHz, DMSO-d_6, 25 °C) δ (ppm): 167.7 (quaternary carbon, C2-thiazole); 160.3 (quaternary carbon, C–F); 158.7 (quaternary carbon, C4-thiazole); 143.3; 140.2 (–CH=N–); 139.9 (quaternary carbon, C9a-carbazole); 129.3, 126.1 (quaternary carbon, C4a, C8a-carbazole); 125.3 (quaternary carbon, C4b-carbazole); 124.7 (quaternary carbon, C3-carbazole); 123.6, 122.3 (quaternary carbon, C1-phenyl); 122.1; 120.6; 119.7; 119.3; 116.1; 115.9; 109.7; 109.4; 108.0; 107.9 (C5-thiazole); 37.1 (–**C**H_2–CH_3); 13.7 (–CH_2–**C**H_3). HR-MS (ESI$^+$): m/z [M + H]$^+$ calcd for $C_{24}H_{19}N_4SF$: 415.1392, found: 415.1392.

*2.2.3.17 4-(3,4-Dichlorophenyl)-2-(2-((9-ethyl-9H-carbazol-3-yl)methylene)hydrazone)thiazole (**4n**).* Chemical formula: $C_{24}H_{18}Cl_2N_4S$; colorless amorphous powder (0.2591 g); yield of 82.63%; melting point: 240–241 °C; R_f = 0.68 (V_{hexane} : $V_{ethyl\ acetate}$ = 7 : 3); IR (λ_{max}, cm^{-1}, KBr): 3237 (–CH stretching vibration); 3050 (–CH_3); 2977 (–CH_2–); 1619 (C=N azomethine, C=N thiazole); 1489 (C=C aromatic); 1233 (C–N aromatic); 1136 (C–N); 934, 752 (aromatic ring bearing substituents); 633 (Ar–Cl). ^{1}H-NMR (500 MHz, DMSO-d_6, 25 °C) δ (ppm): 1.33 (t, J = 6.0 Hz, 3H, –CH_2–C**H**$_3$); 4.47 (q, J = 6.0 Hz, 2H, –C**H**$_2$–CH_3); 7.24 (t, J = 6.3 Hz, 1H); 7.49 (t, J = 6.5 Hz, 1H); 7.54 (s, 1H, H–C5-thiazole); 7.64 (d, J = 6.5 Hz, 1H); 7.63–7.68 (m, 2H); 7.84–7.87 (m, 2H); 8.09 (d, J = 2.0 Hz, 1H, –CH=N–); 8.22 (d, J = 6.5 Hz, 1H); 8.23 (s, 1H); 8.38 (d, J = 1.0 Hz, 1H). ^{13}C-NMR (125 MHz, DMSO-d_6, 25 °C) δ (ppm): 168.6 (quaternary carbon, C2-thiazole); 147.8 (quaternary carbon, C4-thiazole); 143.3 (–CH=N–); 140.2 (quaternary carbon, C9a-carbazole); 139.9; 135.2 (quaternary carbon, C4-phenyl); 131.4 (quaternary carbon, C3-phenyl); 130.8 (quaternary carbon, C1-phenyl); 129.6; 127.1, 126.1 (quaternary carbon, C4a, 8a-carbazole); 125.5 (quaternary carbon, C4b-carbazole); 125.3 (quaternary carbon, C3-carbazole); 122.3; 122.1; 120.6; 119.7; 119.2; 109.7; 109.4; 105.5 (C5-thiazole); 56.0; 37.1 (–**C**H_2–CH_3); 13.7 (–CH_2–**C**H_3). HR-MS (ESI$^+$): m/z [M + H]$^+$ calcd for $C_{24}H_{18}N_4SCl_2$: 465.0707, found: 465.0702.

*2.2.3.18 4-(3-Chloro-4-fluorophenyl)-2-(2-((9-ethyl-9H-carbazol-3-yl)methylene)hydrazone)thiazole (**4o**).* Chemical formula: $C_{24}H_{18}ClFN_4S$; light brown powder (0.2532 g); yield of 83.64%; melting point: 257–258 °C; R_f = 0.63 (V_{hexane} : $V_{ethyl\ acetate}$ = 7 : 3); IR (λ_{max}, cm^{-1}, KBr): 3050 (–CH_3); 2977 (–CH_2–); 1613 (C=N azomethine, C=N thiazole); 1482 (C=C aromatic); 1234, 1135 (C–N); 1087 (Ar–F); 1022 (=N–NH–); 880, 814, 750 (aromatic ring bearing substituents); 676, 614 (Ar–Cl). ^{1}H-NMR (500 MHz, DMSO-d_6, 25 °C) δ (ppm): 1.34 (t, J = 6.0 Hz, 3H, –CH_2–C**H**$_3$); 4.47 (q, J = 6.0 Hz, 2H, –C**H**$_2$–CH_3); 7.24 (t, J = 6.0 Hz, 1H); 7.45–7.50 (m, 3H); 7.64 (d, J = 7.0 Hz, 1H); 7.68 (d, J = 7.5 Hz, 1H); 7.85–7.89 (m, 2H); 8.05 (dd, J_1 = 6.0 Hz, J_2 = 1.5 Hz, 1H, –CH=N–); 8.22 (d, J = 7 Hz, 1H); 8.23 (s, 1H); 8.38 (s, 1H); 12.05 (s, 1H, =N–NH–). ^{13}C-NMR (125 MHz, DMSO-d_6, 25 °C) δ (ppm): 168.6 (quaternary carbon, C2-thiazole); 157.4; 155.5 (quaternary carbon, C–F); 148.1 (quaternary carbon, C4-thiazole); 143.0 (–CH=N–); 140.2 (quaternary carbon, C9a-carbazole); 139.9; 132.7 (quaternary carbon, C1-phenyl); 127.3, 126.1 (quaternary carbon, C4a, 8a-carbazole); 126.0; 125.9; 125.3 (quaternary carbon, C4b-carbazole); 123.5 (quaternary carbon, C3-carbazole); 122.3; 122.1; 120.5 (quaternary carbon, C3-phenyl); 119.8; 119.6; 119.2; 117.2; 117.0; 109.6; 109.4; 104.4 (C5-thiazole); 37.1 (–**C**H_2–CH_3); 13.70 (–CH_2–**C**H_3). HR-MS (ESI$^+$): m/z [M + H]$^+$ calcd for $C_{24}H_{18}N_4SClF$: 449.1003, found: 449.1002.

*2.2.3.19 4-(Benzo[d][1,3]dioxol-5-yl)-2-(2-((9-ethyl-9H-carbazol-3-yl)methylene)hydrazone)thiazole (**4p**).* Chemical formula: $C_{25}H_{20}N_4O_2S$; brown powder (0.2167 g); yield of 72.88%; melting point: 232–233 °C; R_f = 0.56 (V_{hexane} : $V_{ethyl\ acetate}$ = 7 : 3); IR (λ_{max}, cm^{-1}, KBr): 3294 (–CH stretching vibration); 3045 (–CH_3); 2977 (–CH_2–); 1626 (C=N azomethine, C=N thiazole); 1478 (C=C aromatic); 1272 (C–N aromatic); 1237 (C–N aromatic); 1116 (Ar–O–CH_2–); 1046 (=N–NH–); 927 (benzo[*d*][1,3]dioxole); 876, 819 (aromatic ring bearing substituents). ^{1}H-NMR (500 MHz, DMSO-d_6, 25 °C) δ (ppm): 1.34 (t, J = 6.0 Hz, 3H, –CH_2–C**H**$_3$); 4.47 (q, J = 6.0 Hz, 2H, –C**H**$_2$–CH_3); 6.01 (s, 2H, –O–CH_2–O–); 6.95–6.97 (m, 1H); 7.19 (s, 1H, H–C5-thiazole); 7.25 (t, J = 6.3 Hz, 1H); 7.40–7.41 (m, 2H); 7.49 (t, J = 6.3 Hz, 1H); 7.64 (d, J = 6.5 Hz, 1H); 7.68 (d, J = 7.5 Hz, 1H); 7.87 (dd, J_1 = 7.3 Hz, J_2 = 1.3 Hz, 1H); 8.22 (d, J = 6.5 Hz, 1H), 8.25 (s, 1H); 8.38 (d, J = 1.0 Hz, 1H). ^{13}C-NMR (125 MHz, DMSO-d_6, 25 °C) δ (ppm): 168.2 (quaternary carbon, C2-thiazole); 147.6 (quaternary carbon, C3a–O–); 146.8 (quaternary carbon, C7a–O–), 143.3 (–CH=N–); 140.2 (quaternary carbon, C9a-carbazole); 139.9, 126.1 (quaternary carbon, C4a, 8a-carbazole; C5-phenyl); 125.3 (quaternary carbon, C4b-carbazole); 123.6 (quaternary carbon, C3-carbazole); 122.3; 122.0; 120.6; 119.7; 119.4; 119.2; 109.7; 109.4, 108.3; 105.9 (C5-thiazole); 101.9; 101.4 (–O–CH_2–O–); 37.1 (–**C**H_2–CH_3); 13.7 (–CH_2–**C**H_3). HR-MS (ESI$^+$): m/z [M + H]$^+$ calcd for $C_{25}H_{20}N_4SO_2$: 441.1385, found: 441.1388.

*2.2.3.20 2-(2-((9-Ethyl-9H-carbazol-3-yl)methylene) hydrazone)-4-(5-fluoro-2-methoxyphenyl)thiazole (**4q**).* Chemical formula: $C_{25}H_{21}FN_4OS$; light brown powder (0.1896 g); yield of 63.19%; melting point: 261–262 °C; R_f = 0.60 (V_{hexane} : $V_{ethyl\ acetate}$ = 7 : 3); IR (λ_{max}, cm^{-1}, KBr): 3110 (–CH stretching vibration); 3035 (–CH_3); 2972, 2886 (–CH_2–); 1611 (C=N azomethine, C=N thiazole); 1499, 1480 (C=C aromatic); 1242 (Ar–O–CH_3) 1242 (C–N); 1088 (Ar–F); 1033 (=N–NH–); 860, 826, 768 (aromatic ring bearing substituents). ^{1}H-NMR (500 MHz, DMSO-d_6, 25 °C) δ (ppm): 1.34 (t, J = 6.0 Hz, 3H, –CH_2–C**H**$_3$); 3.92 (s, 3H, –O–CH_3); 4.47 (q, J = 6.0 Hz, 2H, –C**H**$_2$–CH_3); 7.12–7.14 (m, 2H, H–C5-thiazole; H–C3-phenyl); 7.24 (t, J_1 = 6.1 Hz, 1H); 7.47–7.50 (m, 2H); 7.64 (d, J = 7.0 Hz, 1H); 7.68 (d, J = 7.0 Hz, 1H); 7.77–7.79 (m, 1H); 7.87 (dd, J_1 = 6.5 Hz, J_2 = 1.5 Hz, 1H); 8.22 (d, J = 6.5 Hz, 1H); 8.25 (s, 1H); 8.38 (s, 1H). ^{13}C-NMR (125 MHz, DMSO-d_6, 25 °C)

δ (ppm): 166.9 (quanternary carbon, C2-thiazole); 155.4 (quanternary carbon, C5-phenyl); 153.0 (quanternary carbon, C2-phenyl); 143.0 (–CH=N–); 140.2 (quanternary carbon, C9a-carbazole); 140.0, 126.1 (quanternary carbon, C4a, 8a-carbazole); 125.4 (quanternary carbon, C4b-carbazole); 123.6 (quanternary carbon, C3-carbazole); 122.3; 122.1; 120.6 (quanternary carbon, C1-phenyl); 119.6; 119.3; 114.9; 114.7; 113.0; 109.7; 109.4; 108.7 (C5-thiazole); 56.0 (–O–CH_3); 37.1 (–CH_2–CH_3); 13.7 (–CH_2–CH_3). HR-MS (ESI^+): *m*/*z* $[M + H]^+$ calcd for $C_{25}H_{21}N_4SOF$: 445.1498, found: 445.1504.

The thiazole derivatives **4a–q** were synthesised *via* a cyclisation reaction between compound (**3**) and various α-bromoketones in ethanol, yielding pure powders characterised by ^{1}H-NMR and ^{13}C-NMR spectra consistent with the expected substituents. All derivatives exhibited a characteristic triplet signal of one proton at around $\delta \sim 7.24$ ppm corresponding to the CH-thiazole moiety, confirming successful thiazole ring closure. The products were obtained in high purity with small melting point variations. However, in several derivatives, the ^{1}H-NMR signal of the =N–NH– proton ($\delta \sim 12$ ppm) disappeared due to its high mobility and possible exchange with protons from the NMR solvent, especially in the presence of trace water. Therefore, future studies on similar derivatives should take note of this proton's instability. The spectral data and yields of each compound are described in the following section.

In principle, reactions between sulfur-containing nucleophiles and α-bromoketones may proceed *via* two competing pathways corresponding to nucleophilic attack by either sulfur or nitrogen at the activated α-carbon center. However, under the present reaction conditions, the sulfur-alkylation pathway is strongly favored. The α-carbon of the α-bromoketone is a soft and highly activated electrophilic site due to the adjacent carbonyl group, making it preferentially susceptible to attack by sulfur, a soft and highly polarizable nucleophile. Moreover, the use of ethanol as a protic solvent significantly reduces the nucleophilicity of nitrogen through hydrogen-bonding interactions, thereby suppressing *N*-alkylation. The absence of strong bases further limits nitrogen activation while having minimal impact on sulfur reactivity. As a result, the reaction proceeds regioselectively *via* initial *S*-alkylation followed by intramolecular cyclization to afford the thermodynamically favored aromatic 1,3-thiazole, consistent with the experimental observation of a single product by TLC and clean ^{1}H and ^{13}C NMR spectra.

The chemical purity of representative compounds **4e**, **4f**, **4g**, and **4l** was evaluated by analytical HPLC prior to biological studies. The HPLC chromatograms (Fig. S102–S105) revealed a single predominant peak for each compound, with relative peak areas of 98.64% (**4e**), 98.66% (**4f**), 95.64% (**4g**), and 94.37% (**4l**), respectively. These results demonstrate that the synthesized compounds possess high chemical purity and confirm that the applied synthetic and purification procedures consistently afford compounds suitable for reliable *in vitro* and *in silico* biological evaluation.

2.2.4. Antibacterial activity. The synthesised compounds were evaluated for their antibacterial and antifungal activities using the agar diffusion method and determination of the minimum inhibitory concentration (MIC). Four standard microbial strains were utilised: *Escherichia coli* ATCC 8739, *Staphylococcus aureus* ATCC 6538, *Salmonella typhimurium* ATCC 14028, and *Candida albicans* ATCC 10231. The agar diffusion test was conducted on Mueller-Hinton agar for bacteria and Sabouraud dextrose agar for fungi, adhering to the guidelines established by the clinical and laboratory standards institute (CLSI). The compounds were solubilised in DMSO and evaluated against chloramphenicol (for antibacterial efficacy) and nystatin (for antifungal efficacy) as positive controls. The MIC values were ascertained using the agar dilution method within a concentration range of *X* to *Y* ppm.[31]

2.2.5. Cytotoxicity assay (SRB method). The cytotoxic activity of the compounds was evaluated using the sulforhodamine B (SRB) assay with slight modifications to a reported procedure. Cells were seeded in 96-well plates at densities of 10 000 cells per well for MCF-7, HepG2, and HeLa, and 7500 cells per well for Human non-small cell lung carcinoma cell line (NCI-H460). After incubation for 24 h, cells were treated with different concentrations of the test compounds and incubated for a further 48 h. The cells were then fixed with cold 50% (w/v) trichloroacetic acid (Merck) for 1–3 h, rinsed with distilled water, and stained with 0.2% (w/v) SRB (Sigma) for 20 min. Excess dye was removed by washing five times with 1% acetic acid (Merck), and the bound dye was solubilised in 10 mM Tris base (Promega).[30] Absorbance was measured at 492 and 620 nm using a Synergy HT microplate reader (BioTek Instruments). The percentage of growth inhibition (Inh %) was calculated using the equation: Inh % $= (1 - [O_{dt}/O_{dc}]) \times 100$, where O_{dt} and O_{dc} represent the optical density values of the test and control samples, respectively. Ellipticine served as the positive control. Cytotoxicity assays were performed in three independent experiments, each conducted with three technical replicates per concentration. IC_{50} values were calculated from the averaged data and are reported as mean ± SD.

2.2.6. Anti-inflammactivity. The anti-inflammatory activity of the synthesised derivatives was evaluated based on their ability to inhibit lipopolysaccharide (LPS)-induced nitric oxide (NO) production in RAW 264.7 macrophage cells. The cells were cultured in Dulbecco's modified eagle medium (DMEM) media supplemented with 10% foetal bovine serum (FBS) and other essential nutrients. After reaching confluence, the cells were pretreated with the test compounds for 2 h, followed by stimulation with LPS (1 μg mL^{-1}) for 24 h. The amount of NO released was indirectly quantified by measuring the accumulation of nitrite (NO_2^-) using the Griess reaction. Briefly, 100 μL of culture supernatant was mixed with 100 μL of Griess reagent, containing sulfanilamide and *N*-(1-naphthyl)ethylenediamine, and the absorbance was measured at 540 nm. Dexamethasone was used as a positive control. The percentage of NO inhibition was calculated relative to the LPS-treated group, and Half-Maximal inhibitory concentration (IC_{50}) values were determined using TableCurve 2D v4.0.[35] To simultaneously assess cell viability under experimental conditions, 3-(4,5-dimethylthiazol-2-yl)-2,5-diphenyltetrazolium bromide assay (MTT assay) was conducted in parallel. After removing the culture medium for NO quantification, 10 μL of MTT solution (5 mg mL^{-1}) was added to each well and incubated for 4 h. The

resulting formazan crystals were dissolved in DMSO, and absorbance was recorded at 540 nm. The percentage of viable cells was calculated relative to the negative control. Anti-inflammatory activity was evaluated using three independent experiments, with each concentration tested in triplicate within each experiment. The results are expressed as mean ± standard deviation (SD), ensuring data reliability and reproducibility.

2.2.7. α-Glucosidase inhibitory activity. The antidiabetic potential of the synthesised derivatives was evaluated through their α-glucosidase inhibitory activity, using *p*-nitrophenyl-α-D-glucopyranoside (*p*NPG) as the substrate. The compounds were initially dissolved in DMSO (20 mg mL^{-1}) and subsequently diluted in phosphate buffer (pH 6.8) to obtain final concentrations ranging from 4 to 500 μg mL^{-1}. Each well of a 96-well microplate contained 50 μL of the test solution, 20 μL of enzyme solution (0.5 U mL^{-1}), and 130 μL of phosphate buffer, followed by incubation at 37 °C for 15 min. The reaction was then initiated by adding 50 μL of pNPG (5 mM) and further incubated for 60 min. The enzymatic reaction was terminated with 80 μL of 0.2 M Na_2CO_3, and the absorbance was measured at 405 nm.[36] Acarbose was used as the positive control. All experiments were performed in triplicate, and the percentage inhibition was calculated based on the optical density values. The IC_{50} values were determined using TableCurve 2D v4.0 to evaluate the α-glucosidase inhibitory efficiency of the tested compounds. α-Glucosidase inhibition was assessed through three independent experiments, with each experiment carried out in triplicate. All data were statistically processed and are presented as mean ± SD.

2.2.8. *In silico* molecular docking, MD simulation and ADMET

2.2.8.1 Molecular docking. The five candidated **4a**, **4e**, **4f**, **4g**, **4l** have conducted *in silico* to 4 file target enzymes: such as 4J5T, 2VF5, 4WCU and 1T8I to explain why compound has exposed inhibits diabetes (4J5T), inhibits cancer (1T8I), inhibits anti-inflammatory (4WCU), antibacterial (2VF5) *in silico*. For docking parameters such as 4J5T.pdb (spacing: 0.600, the numbers of elements (50, 50, 50), and grid box (−18.417, −20.925, 8.009)); 2VF5.pdb: pdb (spacing: 0.500, the numbers of elements (50, 50, 50), and grid box (26.577, 22.697, 8.113)); 4WCU.pdb: (spacing: 0.600, the numbers of elements (50, 50, 50), and grid box (29.286, −59.727, −26.674)); 1T8I.pdb: spacing: 0.600, the numbers of elements (60, 60, 60), and grid box (20.968, 0.667, 41.024)); procedure docking of conformation of compounds: **4a**, **4e**, **4f**, **4g**, **4l** has followed Scheme S1. The coordinations of active center of enzyme has bene detected by Discovery Studio Visualizer software *via* article. The target enzymes before processing docking has been checked the residual amino acid on chains of enzyme by Swiss-pdb viewer software. For one target ezyme has removed the water molecules and heteroatoms and saves as by targer.pdb. For structures of ligands, it is optimized by Avogadro software by MMFF94 force field and saved by *.pdb format before reading to Autodock tool. The parameters of docking processing are examinated and selected depend on size of ligand molecule and saved in dock.gpf file. The docking parameters are selected by the numbers of running of 1000 times, docking method of Genetic Algorithm and out put in file dock.dpf.[37–44]

2.2.8.2 Prediction of drug-likeness and ADMET analysis. The drug-likeness properties and absorption, distribution, metabolism, excretion, and toxicity (ADMET) profiles of the synthesised compounds were evaluated using the online platform ADMETlab2.0. Based on Lipinski's Rule of Five, which serves as a common guideline for predicting oral bioavailability, key physicochemical parameters, such as molecular weight, log *P*, and the number of hydrogen bond donors and acceptors, were analysed. These computational tools offer a preliminary yet dependable understanding of the pharmacokinetic properties and safety of prospective drug candidates, markedly decreasing both time and expense relative to conventional methods.[45]

2.2.8.3 Molecular dynamics (MD) simulation. To assess the stability and long-term interactions between the investigated compounds and their target enzymes, molecular dynamics (MD) simulations were performed using Desmond (Schrödinger LLC) on a Linux environment (Scheme S2). The optimal ligand–protein complex obtained from docking studies was used as the initial input structure. The system was solvated in a TIP3P water model and enclosed in an orthorhombic box with a 10 Å buffer around the complex. It was then neutralised by adding Na^+ or Cl^- ions and adjusted to a physiological salt concentration of 0.15 M. Energy minimisation was performed to remove steric clashes, followed by equilibration under the *NVT* (constant volume and temperature) and *NPT* (constant pressure and temperature) ensembles at 300 K and 1.01325 bar, using the RESPA integrator with a 2 fs time step.[46] The MD simulation was run for 100 nanoseconds (ns) and comprised approximately 63 649 atoms, including the protein, ligand, counter ions, and 16 882 water molecules. The resulting trajectories were analysed to calculate parameters such as root mean square deviation (RMSD), radius of gyration (R_g), and the number of hydrogen bonds between the ligand and protein over time, which provided information about the stability and binding persistence of the ligand within the active site of the target protein.

3. Results and discussion

3.1. Antibacterial activity

The derivatives **4a–q** were evaluated for their inhibitory activity against bacterial and fungal strains, including *Escherichia coli* ATCC 8739, *Staphylococcus aureus* ATCC 6538, *Salmonella typhimurium* ATCC 14028, and *Candida albicans* ATCC 10231. The results showed that compounds **4a**, **4c**, **4e**, **4h**, **4k**, **4n**, **4o**, and **4p** formed clear inhibition zones on agar plates (Fig. S82–S85). In the sterile ring radius measurement test on agar plates, it was found that for *Escherichia coli*, *Staphylococcus aureus*, and *Candida albicans*, compound **4o** at a concentration of 250 μg per well showed the best results with diameters of 8.5 and 10.5 mm, respectively, among the derivatives, while chloramphenicol showed diameters of 22, 26, and 18.8 mm, respectively. For *Salmonella typhimurium*, compounds **4a**, **4e**, **4h**, and **4n** all showed a radius of 8 mm, while chloramphenicol showed a radius of 26 mm. The antibacterial ability, based on the MIC value (Fig. 1), can be compared as follows: **4h** < **4p** < **4o** < **4a** < **4k** < **4c** < **4n** < **4e** < positive control. Compound **4e**, bearing a chloro substituent, demonstrated the highest antibacterial activity

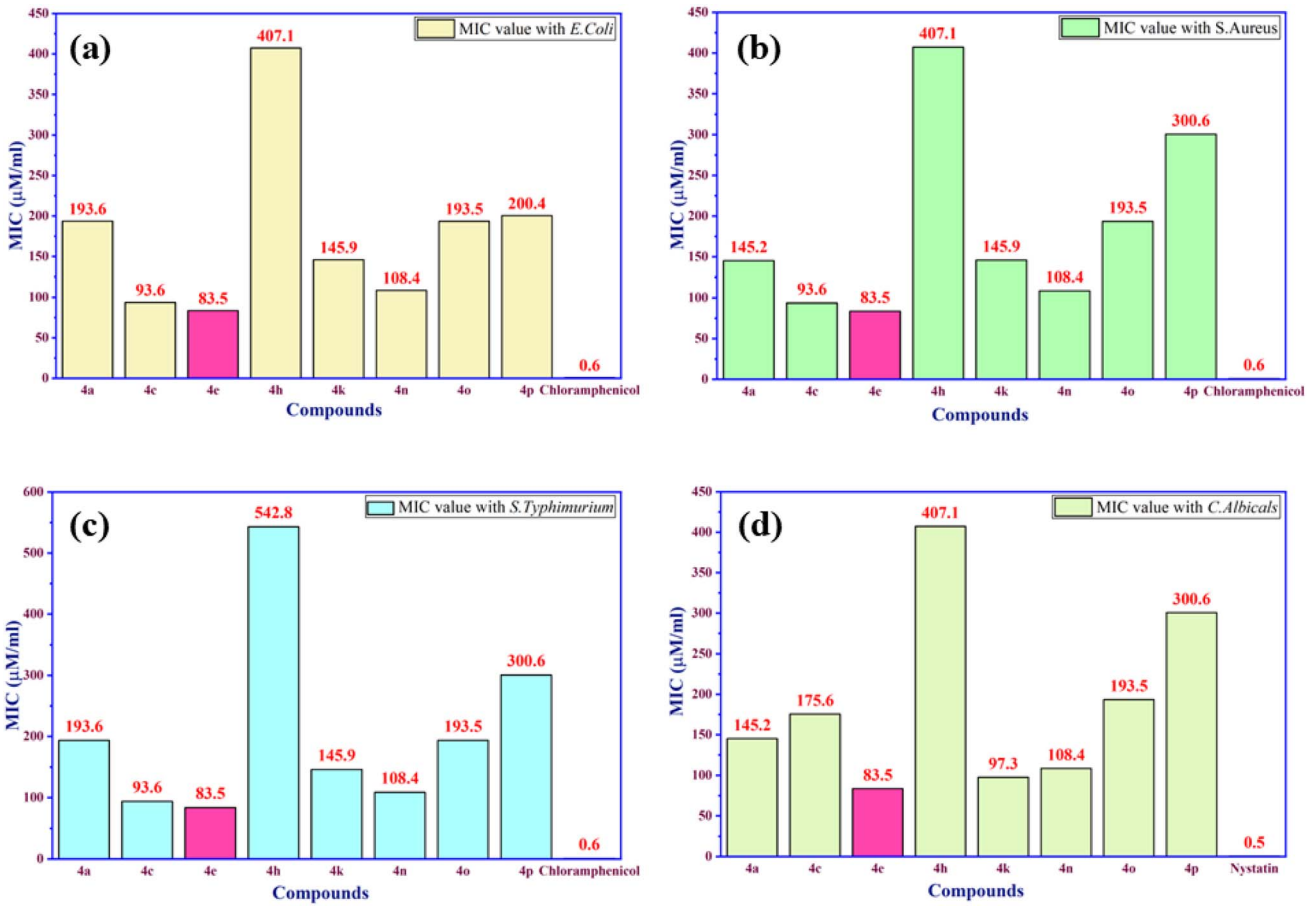

Fig. 1 MIC values of substances exhibiting antimicrobial activity: (a) *Escherichia coli*, (b) *Staphylococcus aureus*, (c) *Salmonella typhimurium*, (d) *Candida albicans*.

within the series, with an MIC = 83.5 μM against the tested bacterial and fungal strains. Although this activity is moderate, it suggests a beneficial contribution of the chlorine atom, likely enhancing membrane interaction and inhibitory behaviour.[47] The antibacterial activity of compound **4e**, when compared with recently reported thiazole derivatives, remains relatively modest. For example, Sateesh Kuna *et al.* (2023) synthesized a series of coumarin-containing thiazole derivatives that showed strong antibacterial activity, with MIC values ranging from 7.69 to 22.76 μM.[48] The lower activity observed for **4e** may reflect limited membrane permeability, indicating that halogenation remains a promising structure–activity relationship optimisation (SAR) direction for designing analogues with improved antibacterial performance.

3.2. Cytotoxic activity

The anticancer activity of the compounds **4a–q** was evaluated against A549, HepG2, and MCF-7 cell lines using the SRB assay, with ellipticine as the reference drug (Fig. S90–S92). Five compounds (**4a**, **4e**, **4g**, **4i**, **4j**) shown significant cytotoxic activity against HepG2 and MCF-7 cell lines. In terms of activity, a comparison based on IC_{50} values can be made as follows: for MCF-7: **4i** < **4j** < **4e** < **4a** < **4g** < ellipticine; for HepG2: **4i** < **4e** < **4j** < **4a** < **4g** < ellipticine; and for A549: **4a** < **4g** < ellipticine (Fig. 2). Compound **4g** showed the most potent cytotoxic activity, with IC_{50} values of 2.6 ± 0.2 μM for HepG2, 6.4 ± 0.7 μM for MCF-7, and 6.6 ± 0.6 μM for A549, although still less active than Ellipticine (IC_{50}: 0.3–0.4 μM). These findings suggest that the nitro substituent present in **4g** may play a critical role in enhancing its affinity toward molecular targets involved in cancer cell proliferation and survival, thereby improving its cytotoxic efficacy.[49] In comparison to prior publications on thiazole-based anticancer medicines, the cytotoxic efficacy of compound **4g** was deemed promising. Hassan *et al.* (2023) reported thiazole derivatives with IC_{50} values of 34–92 μM against A549 and 37–80 μM against MCF-7, relative to erlotinib (IC_{50} = 30 and 40 μM, respectively).[50] Likewise, Kuzu *et al.* (2025) described a structurally distinct thiazole library exhibiting a broad potency range, with IC_{50} values of 9.2–182.2 μM (MCF-7), 25.2–195.7 μM (A549), and 7.2–168.0 μM (HepG2), compared to doxorubicin (IC_{50} = 0.6–1.3 μM).[51] In comparison to the reference data, compound **4g** demonstrated considerable potency, attaining IC_{50} values in the low micromolar range across all examined cell lines. The results indicate that **4g** is a promising lead compound for subsequent optimization studies, especially with adjustments to solubility and cell membrane permeability.

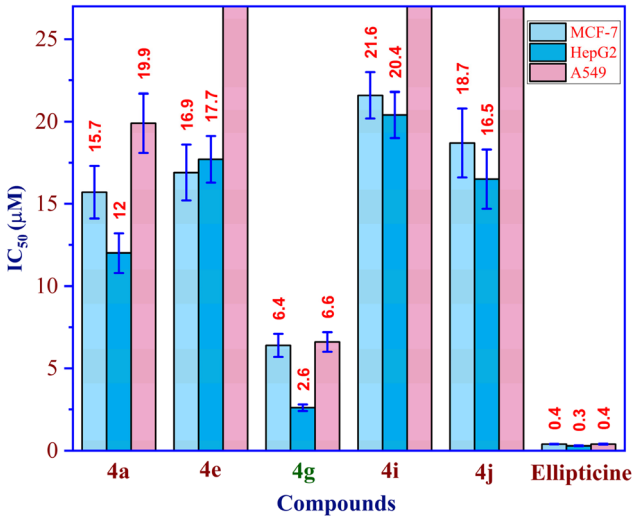

Fig. 2 The IC_{50} values of the derivatives suggest potential toxicity for the three cancer cell lines: MCF-7, HepG2, and A549 analysed.

3.3. Anti-inflammatory activity

The anti-inflammatory activity of the compounds **4a–q** was assessed *via* their ability to suppress nitric oxide (NO) production in LPS-stimulated RAW 264.7 macrophages, using dexamethasone as the reference drug. All compounds exhibited dose-dependent NO inhibition, with seven derivatives (**4a**, **4d**, **4e**, **4f**, **4g**, **4o**, and **4p**) for adequate inhibitory capacity (Fig. S93). The IC_{50} values ranged from 20.5 to 15.4 μM (Fig. 3), while dexamethasone displayed an IC_{50} value of 13.7 ± 1.2 μM. Comparing the anti-inflammatory activity of compounds based on IC_{50} values reveals the following order: **4o** < **4d** < **4p** < **4a** < **4e** < **4f** < dexamethasone. Notably, compound **4f** demonstrated the most potent activity (IC_{50} = 15.4 ± 1.0 μM), comparable to dexamethasone, while maintaining excellent cell viability (99.8% – Fig. S94). From a SAR perspective, the enhanced potency of **4f** can be attributed to the presence of a bromine substituent, which facilitates σ-hole/halogen bonding interactions and improves lipophilicity, thereby supporting membrane penetration and efficient engagement with the iNOS active site.[52]

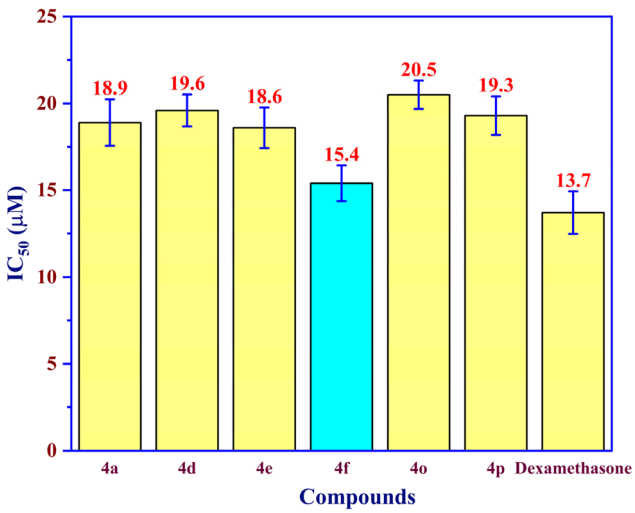

Fig. 3 The IC_{50} values of the derivatives indicate strong inhibition of the inflammatory mediator nitric oxide (NO).

In comparison to previously published thiazole derivatives, the performance of **4f** is favourable. For instance, Fang *et al.* (2024) reported compound **12b** with an IC_{50} of 2.6 μM, which surpasses that of methylprednisolone.[53] While Lin *et al.* (2024) documented thiazole derivatives exhibiting IC_{50} values of 11.0–61.5 μM, compared to dexamethasone (IC_{50} = 21.2 μM).[54] Compound **4f** was recognised as a promising derivative for the development of anti-inflammatory medications, possessing the capacity to refine its structure to augment desired efficacy and solubility.

3.4. α-Glucosidase inhibitory activity

The antidiabetic potential of the synthesised derivatives was evaluated based on their α-glucosidase inhibitory activity using *p*-nitrophenyl-α-D-glucopyranoside (*p*NPG) as the substrate. All compounds demonstrated concentration-dependent inhibitory activity (Fig. S95), with the inhibitory levels ranked by IC_{50} in the following order: **4e** < **4j** < **4o** < **4c** < **4h** < **4m** < **4k** < **4n** < **4q** < **4i** < acarbose < **4a** < **4l**, with values ranging from 436 to 41 μM. Remarkably, compounds **4a** and **4l**, both bearing phenolic hydroxyl groups, exhibited IC_{50} values of 46 ± 2 μM and 41 ± 2 μM, three times more effective than acarbose (117 ± 8 μM). These findings underscore the key contribution of –OH groups in active-site binding, with the additional $-CH_2OH$ moiety in **4l** likely providing an extra hydrogen-bonding interaction, accounting for its enhanced affinity.[55,56]

Comparison with recent studies on thiazole derivatives indicates that the inhibitory potential of compounds **4l** and **4a** is substantial (Fig. 4). Zahra *et al.* (2023) synthesised various thiazole compounds and documented IC_{50} values ranging from 99 to 39 μM, whereas acarbose showed an IC_{50} of 1.21 μM.[57] Khan *et al.* (2023) assembled a variety of thiazole compounds, with IC_{50} values ranging from 18 to 3 μM. Although some derivatives in Khan's series surpassed acarbose, compound **4l** demonstrated threefold more potent inhibition than acarbose under identical assay conditions.[58] Likewise, Seliem *et al.* (2025) reported IC_{50} values of 112–183 μM, compared with acarbose (IC_{50} = 394 μM).[59] However, their work lacked ADMET and MD validation, limiting drug-development insight. The results indicate that compound **4l** represents a promising structure for future antidiabetic drug development targeting type II diabetes.

3.5. Structure–activity relationship (SAR) analysis

Substituents on the phenyl ring at the 4-position of the thiazole core played a pivotal role in modulating the biological activities of the compounds—notably, halogen substituents (Cl, Br) at the *para* position significantly enhanced activity. Compound **4e** (4-Cl) demonstrated the most potent antibacterial effect in the series (MIC = 83.5 μM), while **4n** (3,4-Cl) also exhibited favourable antibacterial properties. These findings suggest that chlorine atoms may enhance membrane interactions and bacterial inhibition by increasing lipophilicity and participating

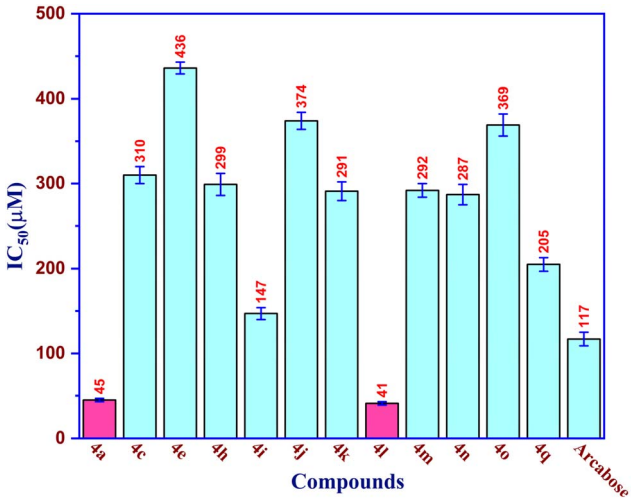

Fig. 4 The IC_{50} values of the derivatives demonstrate significant inhibition of the enzyme α-glucosidase.

in halogen bonding. Similarly, **4f** (4-Br) showed the most pronounced anti-inflammatory activity (IC_{50} ≈ 15.4 μM), comparable to dexamethasone, implying that the bulky bromine substituent may enhance hydrophobic interactions and potentially engage in halogen bonding (σ-hole interactions) with the active site of iNOS.[53] These observations align with previous reports indicating that halogenated derivatives (Cl, Br, I) tend to enhance lipid solubility and facilitate halogen bonding with enzyme carbonyl groups, thereby promoting cell membrane penetration and inhibiting microbial growth.[60]

The nitro group (–NO_2) also proved highly effective, particularly at the *para* position. Compound **4g** (*para*-NO_2) exhibited the lowest IC_{50} values across MCF-7, HepG2, and A549 cell lines, significantly outperforming most other derivatives and closely approaching the potency of ellipticine. This enhancement may stem from the strong electron-withdrawing character of the nitro group, which increases the electrophilicity of the conjugated system and favours interactions with biological targets in cancer cells. In contrast, **4h** (*meta*-NO_2) displayed the weakest antibacterial activity, underscoring the importance of precise substituent positioning to achieve optimal electronic effects.

Hydroxyl-containing derivatives (–OH), particularly those with phenolic or benzylic hydroxyl groups, showed superior α-glucosidase inhibitory activity. Compounds **4a** (*para*-OH) and **4l** (*ortho*-CH_2OH–OH) exhibited IC_{50} values of 46 μM and 41 μM, respectively, markedly outperforming acarbose (117 μM). The phenolic –OH group provides strong hydrogen bonding capability at the enzyme's active site, while the benzylic –CH_2OH moiety in **4l** adds additional hydrogen-bonding interactions with surrounding residues, enhancing complex stability.

Other substituents, including –OCH_3, –CH_3, polycyclic aromatics, –CF_3, and –OCF_3, generally conferred moderate to weak activity. For instance, compounds **4c** (4-OCH_3) and **4k** (4-CH_3) displayed only modest antibacterial or anticancer effects,

Table 1 The most significant molecular docking results were obtained for the interactions between the ligands and the crystal structures of the target enzymes 4J5T: PDB[a], 1T8I: PDB[a], 4WCU: PDB[a], and 2VF5: PDB[a]

Entry	Pose	Free energy of binding[b]	K_i[c]	The number of hydrogen bonds[d]	The property and bond length[d]
4a	283	−8.14	1.08	0	—
4l	612	−8.56	0.53	4	A:Gly312:N-612:O (2.65 Å) A:Lys324:N-612:O (3.11 Å) A:Arg799:N-612:S (3.13 Å) 612:H-A:Leu797:O (2.02 Å)
Small ligand in 4J5T	586	−4.49	513.52	3	586:H-A:Glu374:O (2.13 Å) 586:H-A:Glu374:O (2.45 Å)
Acarbose	926	−0.32	583.93 × 10^6	3	A:Thr281:O-926:N (3.18 Å) 926:H-A:Thr281:O (2.37 Å) 926:H-A:Thr 281:O (2.26 Å)
4g	714	−7.99	1.38	2	A:Arg749:N-714:O (2.90 Å) A:Arg749:N-714:O (3.04 Å)
Small ligand in 1T8I	831	−7.41	3.69	2	831:H-A:Asp301:O (1.74 Å) 831:H-A:Leu 297:O (1.96 Å)
Ellipticine	585	−6.98	7.71	0	—
4f	637	−9.97	0.05	0	—
Small ligand in 4WCU	3	−7.64	4.76	0	—
Dexamethasone	410	−7.18	5.46	1	410:H-B:Pro356:O (1.91 Å)
4e	674	−9.54	0.10	1	X:Ser349:O-674:Cl (3.10 Å)
Small ligand in 2VF5	455	−3.60	2.3 × 10^3	0	—
Chloramphenicol	512	−4.91	251.55	3	X:Gly301:N-512:O (2.81 Å) X:Lys487:N-512:O (2.81 Å) A:512:H-Gly301:O (2.19 Å)

[a] Protein data bank file downloaded from Protein Data Bank. [b] Calculated using AutoDockTools-1.5.6rc3 and reported in units of kcal mol^{-1}. [c] Inhibition constants, K_i, in units of μM, derived from free energy of binding ($\Delta G°$). [d] Based on the Discovery Studio (DSC) 2025 software.

possibly due to their electron-donating nature, which diminishes the electrophilicity of the conjugated system. Similarly, derivatives with weakly electron-withdrawing groups (*e.g.*, **4b**: 4-CF_3 and **4d**: 4-OCF_3) did not show superior activity in any of the biological models tested.

Overall, the SAR trend reveals that electron-withdrawing groups, such as Cl, Br, and NO_2, generally enhance antibacterial, anti-inflammatory, and anticancer activity by promoting strong target binding or favorable pharmacokinetic profiles, while electron-donating groups, especially hydroxyls, are more beneficial for α-glucosidase inhibition due to their capacity for hydrogen bonding. These insights provide a solid rationale for future optimisation, recommending halogenation or nitro substitution for antimicrobial and anticancer development, and retention or enhancement of hydroxyl groups for antidiabetic applications.

3.6. *In silico* docking model

3.6.1. Antimicrobial activity: 2VF5 enzyme. The docking results for compound **4e** at pose 674 demonstrated stable binding within the active site of the target enzyme 2VF5, yielding a binding free energy (ΔG) of −9.54 kcal mol^{-1} and an inhibition constant (K_i) of 0.10 μM, which is significantly superior to the control drug chloramphenicol (Table 1). Notably, **4e** formed a strong hydrogen bond with Ser349 through the chlorine atom (3.10 Å), serving as a key anchoring interaction within the complex. The ligand interaction map (Fig. 5d) indicated that a dense network of van der Waals contacts and several directional steric interactions further reinforced the binding stability of **4e**.

At the structural level, the functional groups of **4e** played different roles in keeping the stable shape. The hydrogen-bonding moiety that directly interacted with Ser349 served as the primary anchoring site. The peripheral aromatic capping group formed amide-π stacking with Lys487, π-alkyl interactions with Leu601 and Arg599, and a bridging van der Waals connection through the connecting unit with Leu601. Additionally, a π-anion hydrophilic interaction with Glu488 contributed to the overall structural stabilisation of the ligand–protein complex. The *in silico* docking results indicate that compound **4e** exhibits a favourable binding affinity toward the target enzyme 2VF5, reflecting its potential for effective enzyme–ligand interactions at the molecular level. However, the

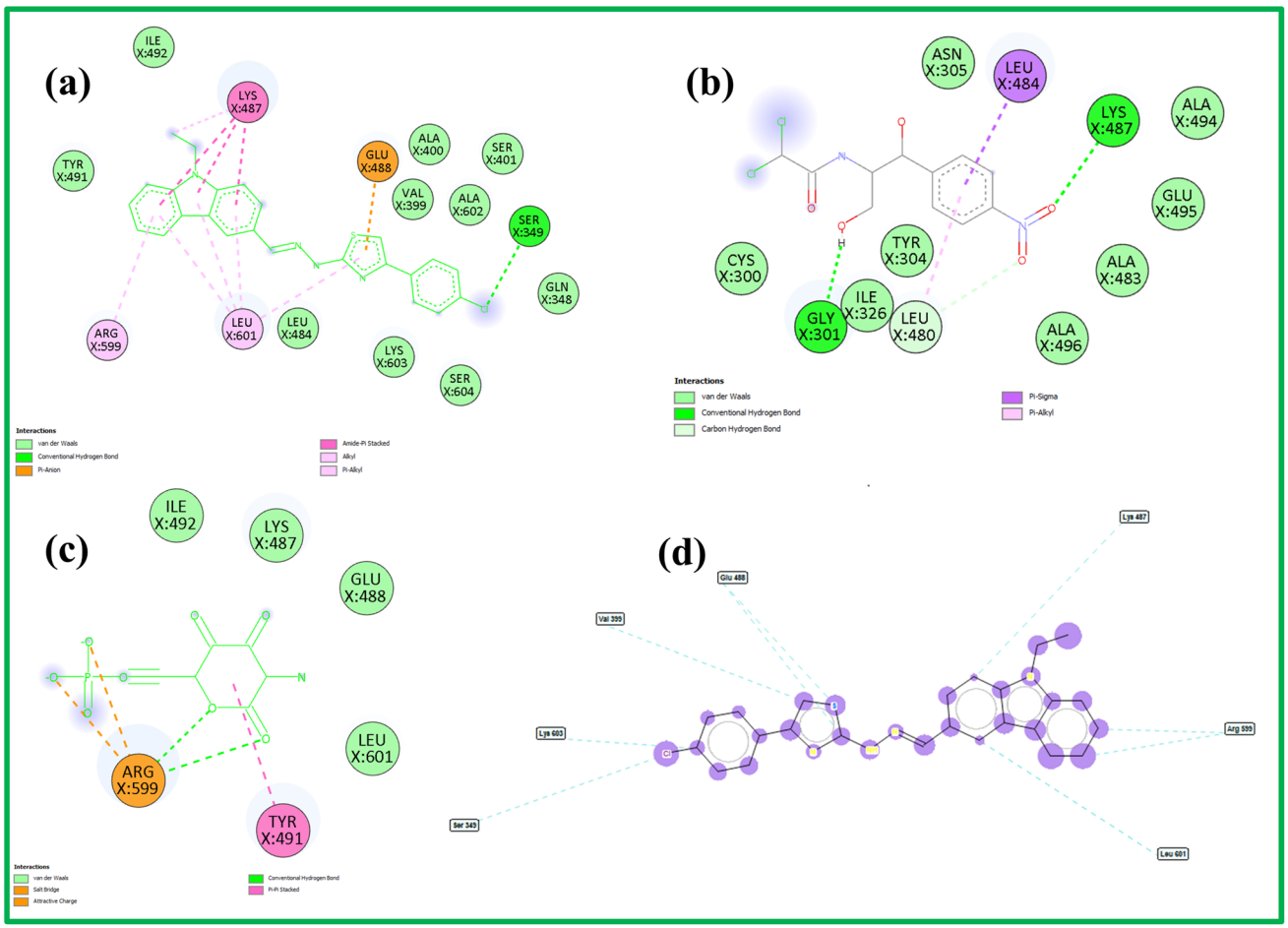

Fig. 5 (a) The 2D interaction model of **4e** or pose 674 with 2VF5, (b) the 2D interaction model of chloramphenicol with 2VF5 (c) the 2D interaction model of the small ligand in 2VF5 with 2VF5 (redocking), (d) the ligand map of **4e**, which the includes steric interactions (blue lines) and the overlap interactions (circles, purple) with 2VF5 enzyme.

in vitro results reveal that the MIC value of **4e** remains higher than that of chloramphenicol. This discrepancy suggests that a strong binding affinity predicted by docking does not necessarily translate directly into optimal antibacterial efficacy under biological conditions, most likely due to extra-enzymatic factors such as limited bacterial membrane permeability or insufficient intracellular transport efficiency. Therefore, in this study, molecular docking is primarily employed to elucidate trends in molecular interactions and to support SAR analysis, while also indicating that the structural scaffold of **4e** represents a promising framework that requires further optimisation, particularly aimed at improving membrane permeability, to enhance its *in vitro* antibacterial activity.

3.6.2. Cytotoxicity: 1T8I enzyme. The docking results indicated that compound **4g** at pose 714 exhibited stable binding to enzyme 1T8I, with a binding free energy (ΔG) of −7.99 kcal mol^{-1} and an inhibition constant (K_i) of 1.38 μM, corroborated by a varied interaction network (Fig. 6a). This configuration established two directional hydrogen bonds with Arg749, which effectively anchored the polar functional groups of the molecule within the active site. Compared with ellipticine (Fig. 6b), compound **4g** exhibited a highly similar interaction pattern, including characteristic π–π stacking interactions, which confirms the reliability of the molecular docking results. Furthermore, the small-molecule structure within 1T8I (Fig. 6c) reproduced the representative interactions of the catalytic pocket, serving as a reference for comparison with the studied ligand. Remarkably, the ligand interaction map of **4g** (Fig. 6d) illustrates the cooperative contribution of steric interactions (green lines), hydrogen bonds (orange lines), and van der Waals contacts (purple circles), confirming that this compound simultaneously exploits both electrostatic and hydrophobic forces to stabilise the binding pose. Structurally, the nitro functional groups of **4g** directly participate in forming two stable hydrogen bonds with Arg749, serving as key anchoring points that secure the molecule within the active cavity. The capping group, consisting of an extended aromatic framework, engages in T-shaped π–π interactions with Trp203 and His346, as well as π-alkyl contacts with Lys347 and His346, which reinforce the overall configuration and enhance binding selectivity. The connecting unit, composed of the central aromatic linker between the functional and capping groups, exhibits extensive van der Waals interactions with neighbouring hydrophobic residues, as well as stabilising π-alkyl interactions

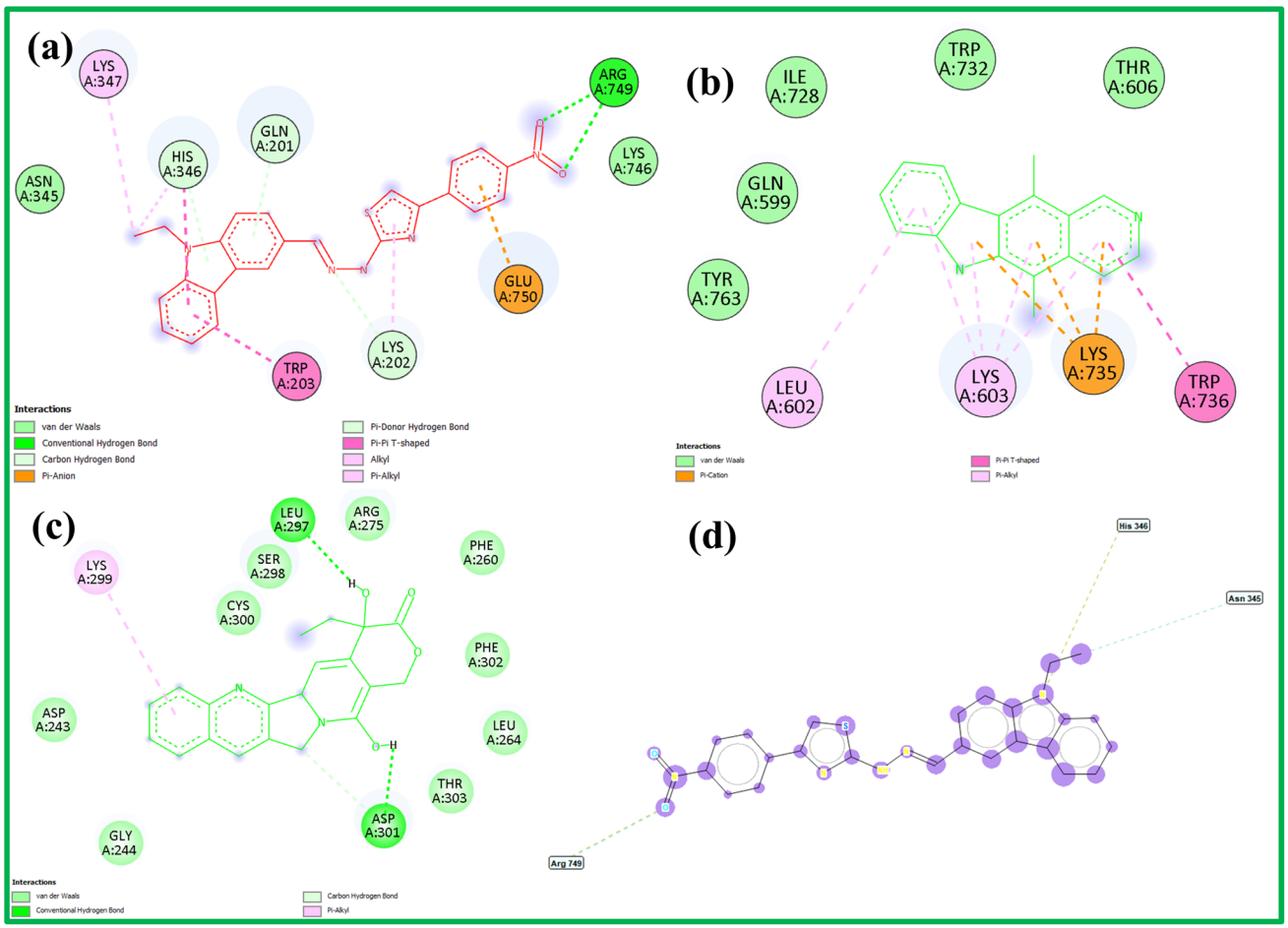

Fig. 6 (a) The 2D interaction model of **4g** or pose 714 with 1T8I, (b) the 2D interaction model of ellipticine with 1T8I (c) the 2D interaction model of the small ligand in 1T8I with 1T8I (redocking), (d) the ligand map of **4g**, which includes the steric interactions (blue lines), the hydrogen interactions (orange lines), and the overlap interactions (purple circles) with 1T8I enzyme.

with Lys202 and π-anion contacts with Glu750, thereby maintaining the rigidity of the ligand scaffold. Compound **4g** exhibited a favourable binding mode within the active site of enzyme 1T8I, as evidenced by its low docking binding energy and a stable interaction network. Notably, this predicted binding behaviour is consistent with the experimental cytotoxicity data, with IC_{50} values of 2.6 ± 0.2 μM for HepG2, 6.4 ± 0.7 μM for MCF-7, and 6.6 ± 0.6 μM for A549, indicating that the enhanced enzyme–ligand interactions contribute significantly to the superior cytotoxic activity of **4g** compared with other derivatives in the same series. Although ellipticine remains more potent *in vitro*, the docking results suggest that **4g** adopts a comparable interaction pattern within the catalytic pocket; the reduced cellular activity of **4g** relative to ellipticine may therefore be associated with differences in inhibition mechanisms or lower cellular membrane permeability. Overall, these findings support the identification of **4g** as a promising lead scaffold for the development of enzyme-targeted anticancer agents in future studies.

3.6.3. Anti-inflanmatory: 4WCU enzyme. The docking results of compound **4f** at pose 637 with the enzyme 4WCU demonstrated a highly stable binding conformation (ΔG = −9.97 kcal mol^{-1}; K_i = 0.05 μM), significantly stronger than that of dexamethasone (pose 410; ΔG = −7.18 kcal mol^{-1}; K_i = 5.46 μM) and the co-crystallised ligand (ΔG = −7.64 kcal mol^{-1}; K_i = 4.76 μM) (Table 1). Notably, compound **4f** did not form any classical hydrogen bonds, whereas dexamethasone established a single hydrogen bond with Pro356:O (1.91 Å). The ligand interaction map of **4f** (Fig. 7d) revealed a dense network of van der Waals interactions (purple circles) together with steric and geometric fitting interactions (green lines) distributed along the aromatic backbone, which rationalises its strong binding affinity in the absence of H-bonds. The 2D interaction diagrams (Fig. 7a) further indicated that **4f** primarily exploits π–π and π-alkyl interactions with aromatic residues (multiple Phe/Tyr) and π-sulfur contacts with Phe340, supplemented by extensive van der Waals interactions that collectively reinforce the binding pose. From a structural standpoint, the functional groups of **4f**, comprising aromatic rings and a bromine substituent, are not oriented for substantial hydrogen donation or acceptance; yet, they provide an extended π-surface, enabling π–π interactions with Phe432 and Phe372, π-alkyl contacts with Tyr329, and enhanced polarisability for van der Waals stabilization. The capping groups (terminal aromatic rings) occupy two

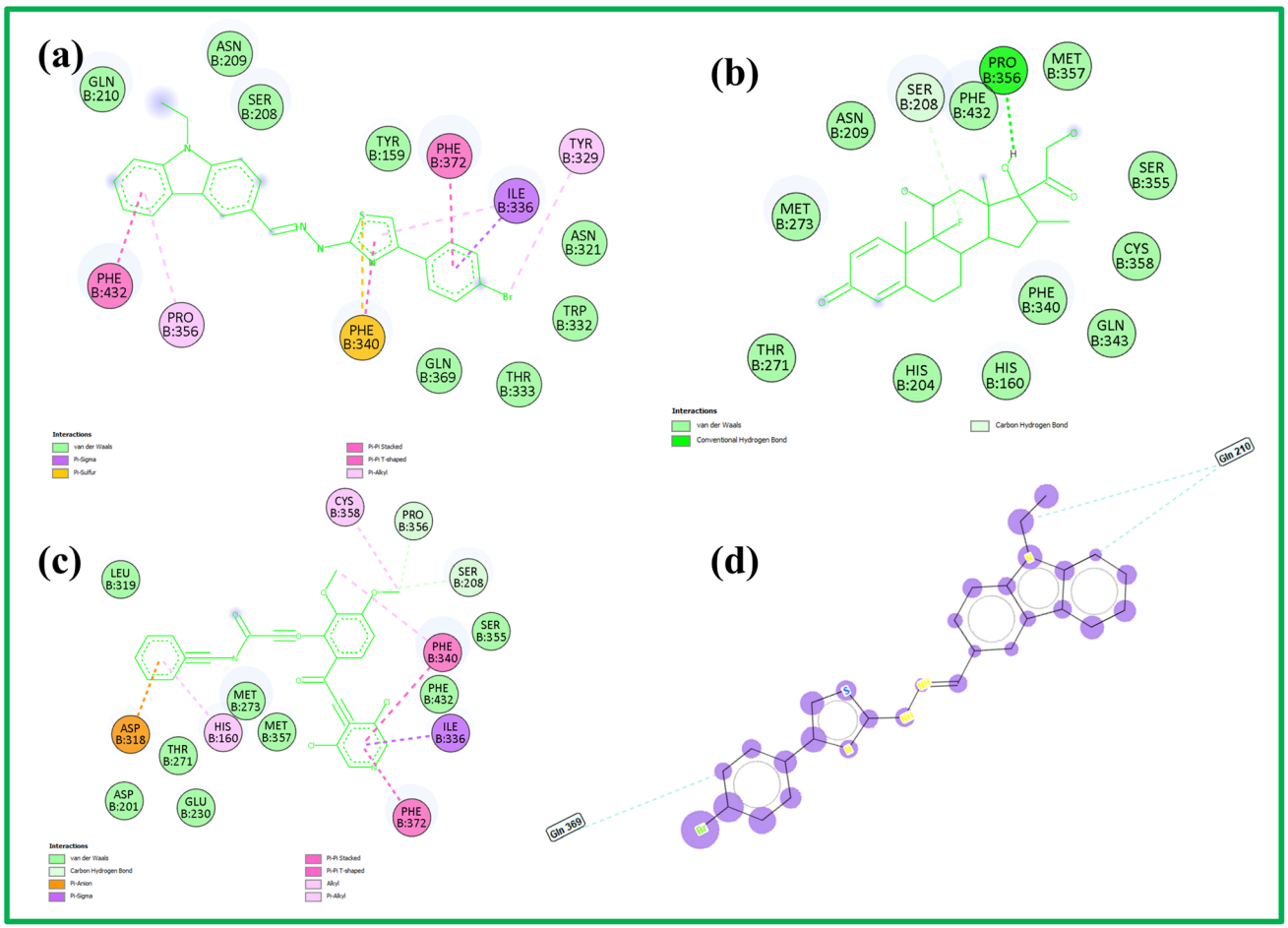

Fig. 7 (a) The 2D interaction model of **4f** or pose 637 with 4WCU, (b) the 2D interaction model of dexamethasone with 4WCU (c) the 2D interaction model of the small ligand in 4WCU with 4WCU (redocking), (d) the ligand map of **4f**, which includes steric interactions (blue lines) and overlap interactions (circles, purple) with 4WCU enzyme.

subpockets, forming multiple T-shaped π–π interactions with Phe432 and Phe372, as well as π-alkyl contacts with Pro356, effectively "locking" the binding conformation. The connecting unit maintains a slender and planar geometry that supports extensive van der Waals dispersion while also engaging in π-sulfur interactions with Phe340 and other hydrophobic residues, thereby stabilising the entire pose. Compound **4f** exhibited a highly favourable docking binding energy (large negative ΔG°), indicating strong and stable interactions with the target enzyme 4WCU in the *in silico* model. This predicted binding behaviour is consistent with the pronounced anti-inflammatory activity observed experimentally, as **4f** displayed an IC_{50} value of 15.4 ± 1.0 μM, which is comparable to that of the reference drug dexamethasone ($IC_{50} = 13.7 \pm 1.2$ μM). Although the docking results suggest a higher binding affinity of **4f** relative to dexamethasone, its *in vitro* activity is slightly lower, implying that factors beyond enzyme–ligand interactions, such as cell membrane permeability and pharmacokinetic properties, may attenuate the biological efficacy compared with docking predictions. Nevertheless, the overall consistency between the docking results and the experimental bioactivity supports the relevance of the docking model in rationalising the observed SAR. Collectively, these findings highlight compound **4f** as a promising lead scaffold for the development of novel anti-inflammatory agents, particularly upon further optimisation of its pharmacological properties.

3.6.4. α-Glucosidase inhibition: 4J5T enzyme. The docking results indicated that both derivatives **4a** and **4l** demonstrated stable binding to the enzyme 4J5T *via* a varied molecular interaction network, as depicted in Fig. 8. Compound **4a** at pose 283 exhibits a $\Delta G^{\circ} = -8.14$ kcal mol^{-1} ($K_i = 1.08$ μM), while compound **4l** at pose 612 has a $\Delta G^{\circ} = -8.56$ kcal mol^{-1} ($K_i = 0.53$ μM) and establishes 4 hydrogen bonds (Fig. 8a and b). To validate the reliability of the docking model, comparisons were made with the co-crystallised ligand 4J5T (Fig. 8c) and the standard inhibitor acarbose (Fig. 8d), which demonstrated that the simulated poses successfully reproduced the characteristic binding features of known α-glucosidase inhibitors. Notably, the ligand interaction map of compound **4l** (Fig. 8e) highlighted three dominant interaction types: steric (blue lines), hydrogen bonds (orange lines), and van der Waals interactions (purple circles), illustrating the synergistic contribution of both hydrophilic and hydrophobic forces to the stabilisation of the binding pose. At the structural level, the functional groups of **4l**, particularly hydroxyl and methylene hydroxyl moieties, directly participated in forming strong hydrogen bonds with hydrophilic residues Gly312, Lys324, and Leu797, which act as anchoring points to retain the molecule in the active site. The capping group, comprising a peripheral aromatic scaffold, primarily engages in π-alkyl, π–π stacking, and π-cation interactions with hydrophobic residues such as His803, Ile734, Pro731, and Arg727, thereby shielding and orienting the molecule at the entrance of the catalytic pocket. The connecting unit, a conjugated aromatic linker bridging the capping group and functional groups, maintained optimal geometric spacing while contributing additional stabilizing interactions, such as π–π stacking and hydrogen bonding with Arg799, as well as van der Waals contacts that reinforced the overall pose stability. The *in silico* docking results indicate that both compounds **4a** and **4l** are capable of forming favourable and stable binding modes within the active site of enzyme 4J5T, as reflected by their low binding energies and well-defined interaction networks, particularly involving directional hydrogen bonding. This trend is in good agreement with the *in vitro* findings, as both compounds exhibited strong and comparable α-glucosidase inhibitory activity, with IC_{50} values of 46 ± 2 μM for **4a** and 41 ± 2 μM for **4l**, mawhich is markedly superior to that of the reference inhibitor acarbose ($IC_{50} = 117 \pm 8$ μM). The qualitative consistency between the docking predictions and the experimental data suggests that the presence of hydroxyl functionalities plays a key role in enhancing enzyme binding affinity through the formation of hydrogen bonds with polar residues in the active site. In the docking models, both **4a** and **4l** effectively exploit these hydrogen-bonding interactions, which rationalize their pronounced inhibitory activity observed *in vitro*. The slightly higher potency of **4l** relative to **4a** may be attributed to the additional –CH_2OH group, which can provide secondary hydrogen-bonding interactions; however, this difference remains modest and is fully consistent with the closely comparable IC_{50} values of the two compounds. Overall, the docking results in this study show good qualitative agreement with the experimental biological data, particularly in capturing activity trends rather than predicting absolute IC_{50} values. Accordingly, molecular docking serves as a supportive tool for rationalising the observed SAR and elucidating the contribution of hydroxyl-containing substituents to α-glucosidase inhibition.

3.6.5. ADMET model. Compound **4l** exhibits an overall favourable ADMET profile (Tables S1–S8), suitable for preclinical development, although several properties require further optimization. In terms of physicochemical characteristics, **4l** possesses a molecular weight of 442.15, topological polar surface area (TPSA) of 82.67 Å^2, and five hydrogen-bond donors/acceptors, all within the acceptable limits of Lipinski's and Veber's rules, suggesting good membrane permeability and absorption potential. Moreover, the compound satisfies most Ghose and Egan criteria, with only a slightly high log P (5.9) that can be mitigated through structural modification or formulation strategies. Its drug-likeness risk score (RSK) composite and synthetic accessibility (SAscore = 2.5) indicate practical synthetic feasibility and the potential for scaffold optimisation.[61,62] Regarding the ADMET properties, **4l** shows moderate absorption, with predicted Caco-2 permeability and low human intestinal absorption (HIA), attributed mainly to its high lipophilicity and poor solubility ($\log S = -7.6$). These limitations are, however, addressable through salt formation or prodrug approaches. The distribution profile indicates strong plasma protein binding (PPB = 100%) and a moderate volume of distribution, consistent with peripheral drug behavior. The low blood–brain barrier (BBB) permeability is advantageous for non-central nervous system (CNS) targets. In metabolic predictions, **4l** is anticipated to interact with specific CYP isoforms (CYP1A2, 2C9, 2D6), a characteristic prevalent in thiazole scaffolds that can be mitigated through substituent optimization. The excretion rate appears moderate, suggesting no rapid

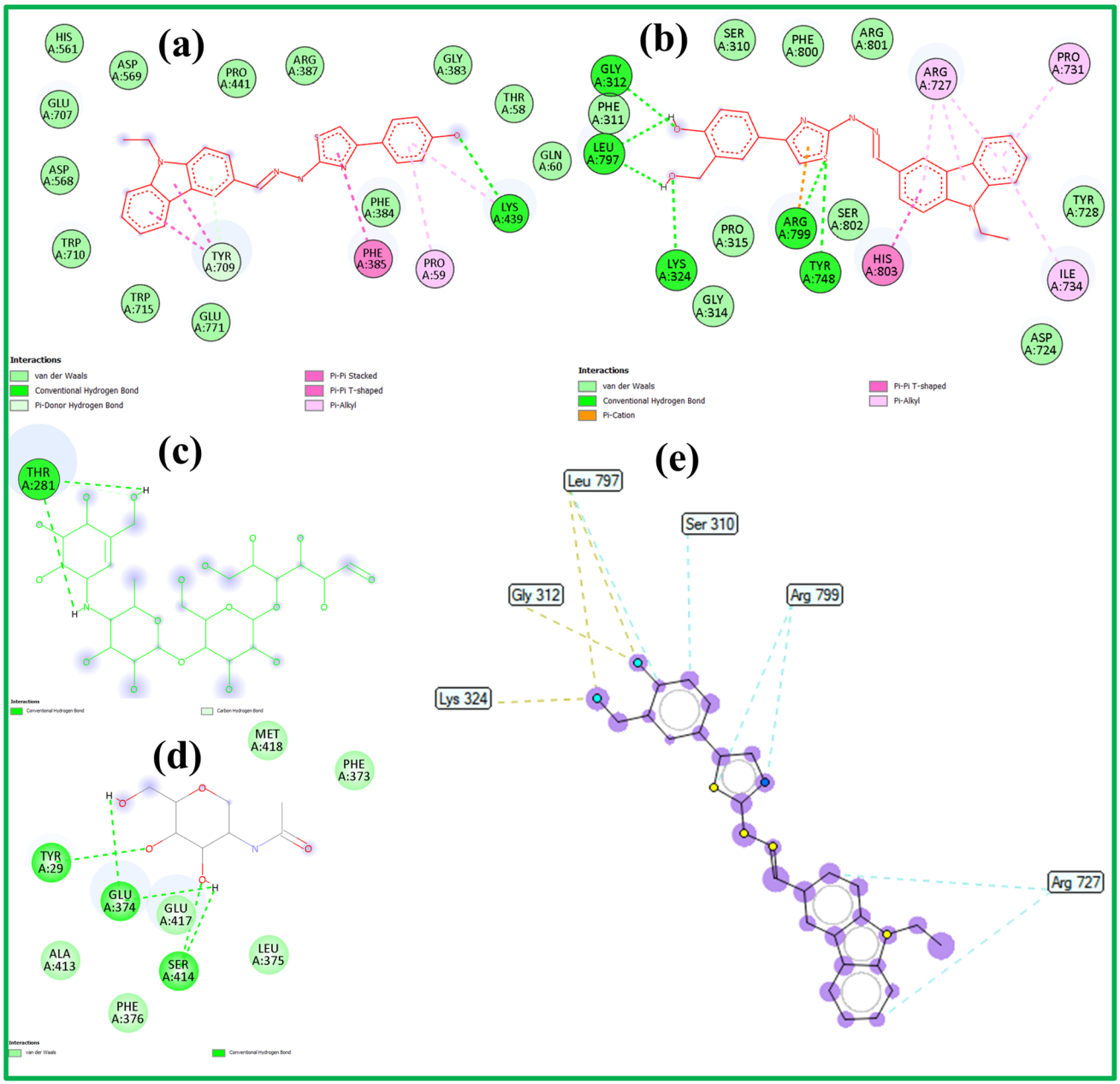

Fig. 8 (a) The 2D interaction model of **4a** or pose 283 with 4J5T, (b) the 2D interaction model of **4l** of pose 612 with 4J5T, (c) the 2D interaction model of the small ligand in 4J5T with 4J5T (redocking), (d) the 2D interaction model of Arcabose with 4J5T (e) the ligand map of **4l**, which includes steric interactions (blue lines), hydrogen interactions (orange lines), and overlap interactions (circles, purple) with 4J5T enzyme.

clearance or abnormal accumulation. Toxicologically, we predict potential drug-induced liver injury (DILI) and Ames-positive alerts. Still, the absence of pan-assay interference compounds (PAINS) and low hERG inhibition probability suggests minimal cardiotoxic liability. Overall, **4l** can be considered a promising and synthetically accessible scaffold that complies with most classical drug-likeness rules. With rational optimization of lipophilicity, sulfur reactivity, and solubility, it holds potential for advancement toward a viable drug candidate[63–66]

3.6.6. Molecule dynamics (MD). Molecular dynamics (MD) analysis of **4l**/pose 612 with the 4J5T enzyme (**4l-4J5T** complex) over 100 ns showed that the complex reached a distinct dynamic equilibrium state after the initial equilibration phase. The root mean square deviation (RMSD) of the enzyme increased rapidly from approximately 1.7 Å to 2.8 Å within the first 15 ns and subsequently stabilised around 2.4–2.6 Å for the remainder of the simulation, indicating that the tertiary structure of α-glucosidase was well preserved, with fluctuations primarily localised to peripheral loop regions (Fig. 9a). In contrast, the ligand RMSD exhibited larger fluctuations, rising from 2.5 Å to 6.8 Å around 40 ns before stabilising at 4.5–5.5 Å, reflecting a non-disruptive repositioning process within the binding pocket (Fig. 9a). This behaviour suggests that, after an initial

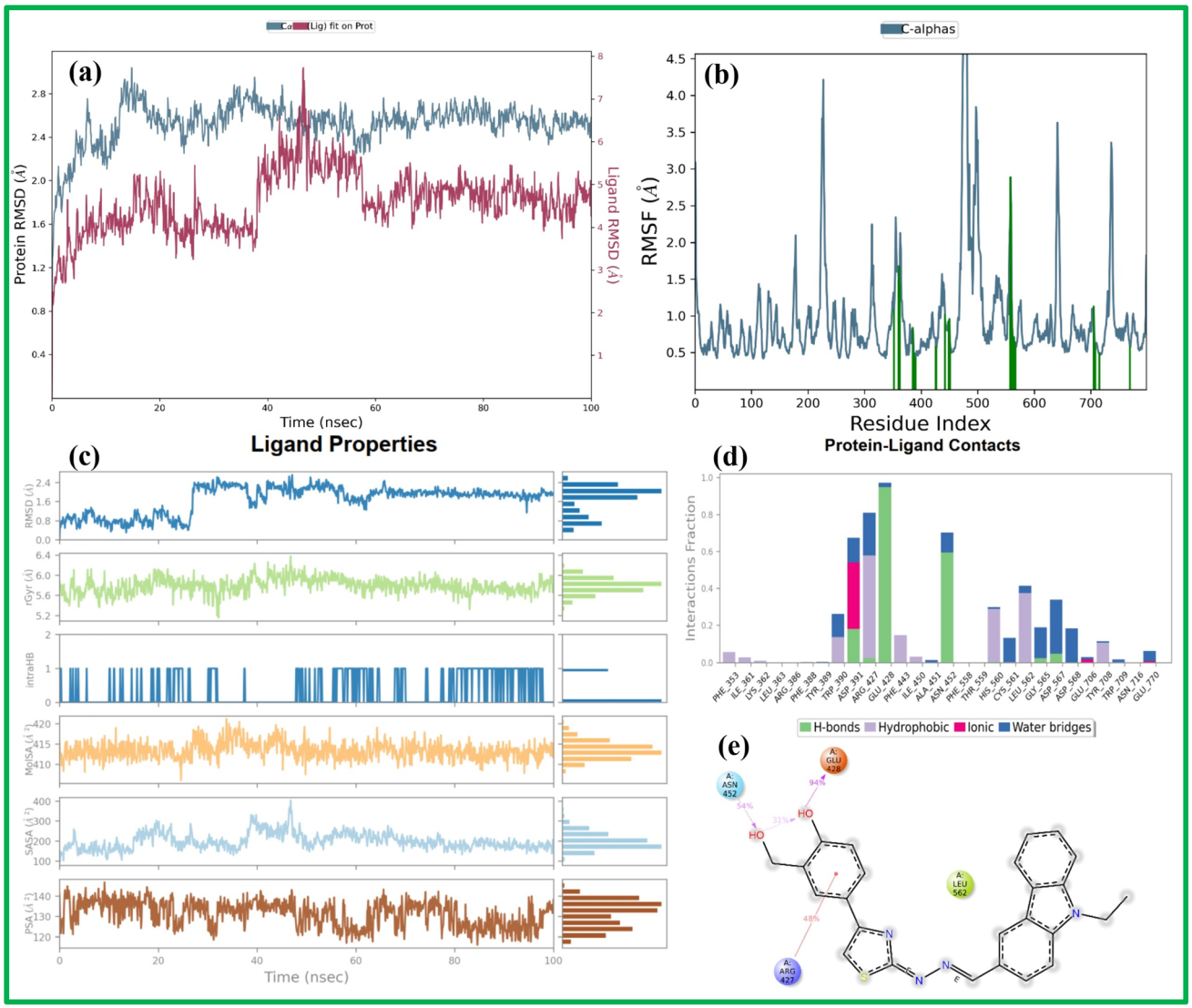

Fig. 9 Molecular dynamics (MD) analysis of the 4l–4J5Tcomplex (4l/pose 612 and 4J5T: pdb): (a) RMSD evolution of protein and ligand; (b) RMSF of the enzyme Cα atoms; (c) Time evolution of key ligand properties; (d) Enzyme–ligand contact profile during the simulation; (e) Representative 2D interaction diagram of ligand 4l/pose 612 and 4J5T: pdb binding site.

conformational adjustment, the ligand adopted a tightly anchored and energetically favourable pose, implying a "breathing" dynamic motion within the pocket without dissociation from the enzyme. The overall system stability was further supported by the root mean square fluctuation (RMSF) analysis (Fig. 9b), in which distal loop residues (around positions 200 and 500) displayed higher fluctuations (6–7 Å), whereas residues within the active pocket, such as Glu428, Asn452, and Asp391, maintained low RMSF values (1–2 Å). This pattern suggests that the catalytic site is structurally rigid, while the edges are flexible, allowing the binding region to adapt to changes in shape while maintaining its integrity.[67] The hydrogen-bonding network exhibited remarkable stability during the simulation, with Glu428 (51.95%) and Asn452 (32.66%) serving as the principal anchoring residues, collectively constituting over 85% of the total hydrogen-bond interactions. In comparison, Asp391 contributed around 10% in a supportive capacity. The combination of the negatively charged carboxylate group of Glu428 and the flexible amide group of Asn452 established robust donor–acceptor hydrogen bonds that effectively stabilised the ligand within the binding pocket, explaining the subsequent stabilisation of the ligand's RMSD. The binding free energy obtained from molecular mechanics-generalized born surface area (MM-GBSA) analysis ranged from −35 to −53 kcal mol^{-1}, reaching a minimum of −53 kcal mol^{-1} around 40 ns, coinciding with the time point at which the ligand adopted its tightest binding conformation, and fluctuating around −42 kcal mol^{-1} during equilibrium. This study confirms a thermodynamically favourable binding process. The correlation between ΔG fluctuations and RMSD/SASA (Solvent accessible surface area) profiles indicated that transient ligand repositioning events did not disrupt key stabilising interactions (Fig. S96–S101). The morphological parameters of the ligand further supported these observations:

the polar surface area (PSA) remained stable between 120 and 140 Å^2 (Fig. 9c), and the radius of gyration (rGyr) stabilised around 5.8 Å, reflecting a compact and minimally deformed conformation. The SASA showed a significant change, reaching a peak of about 300 Å^2 between 40 and 50 ns. This was because the ligand temporarily expanded and was more exposed to the solvent. It then dropped to about 150 Å^2, showing that the ligand temporarily changed its position in the pocket but eventually returned to a "buried" state (Fig. 9c). The coherence among PSA, rGyr, SASA, and $\Delta G°$ variations strongly supports that compound **4l** maintains a stable conformation, tightly bound within the 4J5T active site through a persistent hydrogen-bonding network complemented by hydrophobic interactions. These findings confirm that the **4l-4J5T** complex achieves both dynamic stability and thermodynamic favourability throughout the molecular dynamics simulation.[68]

4. Conclusion

This study reports the successful synthesis and structural confirmation of a series of thiazole derivatives, characterised by NMR, FT-IR, and HR-MS analyses. Among them, compound **4e** showed the most potent antibacterial activity (MIC = 83.5 μM), while **4g** exhibited potent cytotoxicity (IC_{50} = 2.6–6.6 μM). Compound **4f** displayed notable anti-inflammatory effects (IC_{50} = 13.4 μM), comparable to dexamethasone. Remarkably, **4a** and **4l** (–OH, –CH_2OH) showed superior α-glucosidase inhibition (IC_{50} = 45 and 41 μM) to acarbose (117 μM). The molecular docking studies revealed that the ligands exhibited favorable interactions with the respective enzymes. This indicates that the favourable interactions observed *in silico* align with the positive activities seen *in vitro*. The molecular dynamic simulations, spanning 100 ns, demonstrated structural stability, with critical residues such as Glu428 and Asn452 exhibiting hydrogen bond occupancy exceeding 80%. The ADMET profile of compound **4l** adheres to the principles of drug-likeness. Subsequent research endeavors could focus on the structural optimization and augmentation of hydrophilicity to enhance the bioavailability of the synthesized compounds, alongside *in vivo* assessments of compound **4l** in relation to α-glucosidase activity.

Author contributions

Nguyen Duy Khanh: conceptualization, formal analysis, investigation, data curation, writing – original draft, visualization, funding acquisition. Nguyen Thi Hong Anh: formal analysis, investigation, data curation, visualization. Nguyen Thi Mai Tho: methodology, software, validation, writing – review & editing, supervision. Tran Nguyen Minh An: methodology, software, validation, formal analysis, resources, writing – review & editing, supervision, project administration. Nguyen Van Son, Nguyen Thi Nhat Thang: visualization, funding acquisition, data curation. Tran Thuy Quyen: methodology.

Conflicts of interest

There are no conflicts to declare.

Data availability

All experimental and computational data supporting the findings of this study, including *in vitro* bioassay results, molecular docking data, molecular dynamics simulations, ADMET screening, and ^{1}H-NMR, ^{13}C-NMR, FT-IR, HPLC, and HR-MS spectra for structural confirmation, are provided in the manuscript and the supplementary information (SI). Additional raw data are available from the corresponding author upon reasonable request. Supplementary information is available. See DOI: https://doi.org/10.1039/d5ra08472e.

Acknowledgements

This research is funded by Vietnam National Foundation for Science and Technology Development (NAFOSTED) under grant number 104.01-2023.78. The authors also express their sincere appreciation to the Laboratory of the Faculty of Chemical Engineering (FCE), Industrial University of Ho Chi Minh City (IUH), Ho Chi Minh City, Vietnam, for providing essential facilities and technical assistance during the research.

References

1 D. Ungureanu, B. Tiperciuc, C. Nastasă, I. Ionuț, G. Marc, I. Oniga and O. Oniga, *Pharmaceutics*, 2024, **16**, 89.
2 K. H. Narasimhamurthy, T. R. Swaroop and K. S. Rangappa, *Eur. J. Med. Chem. Rep.*, 2024, **12**, 100225.
3 A. F. Kassem, R. H. Althomali, M. M. Anwar and W. I. El-Sofany, *J. Mol. Struct.*, 2024, **1303**, 137510.
4 W. A. A. Fadaly, A. Elshewy, M. T. M. Nemr, K. Abdou, A. M. Sayed and N. M. Kahk, *Bioorg. Chem.*, 2024, **152**, 107760.
5 A. Singh, D. Malhotra, K. Singh, R. Chadha and P. M. S. Bedi, *J. Mol. Struct.*, 2022, **1266**, 133479.
6 H. Aziz, *J. Mol. Liq.*, 2025, **424**, 127064.
7 S. Basak, A. Murmu, B. W. Matore, P. P. Roy and J. Singh, *Eur. J. Med. Chem. Rep.*, 2024, **11**, 100160.
8 Salahuddin, A. Mazumder, M. J. Ahsan, R. Kumar, Z. Ullah, M. Shahar Yar and K. Shabana, *Bioengineering*, 2025, **12**, 1024.
9 J. Liu and L.-N. Wang, *Cochrane Database Syst. Rev.*, 2023, **2023**(1), DOI: 10.1002/14651858.CD010693.pub6.
10 L. Maram, J. M. Michael, H. Politte, V. S. Srirama, A. Hadji, M. Habibi, M. O. Kelly, R. T. Brookheart, B. N. Finck, L. Hegazy, K. S. McCommis and B. Elgendy, *Eur. J. Med. Chem.*, 2025, **283**, 117150.
11 Z. Xu, D. Wu, C. Fang and Y. Li, *Des. Monomers Polym.*, 2023, **26**, 90–105.
12 S. A. Patil, S. A. Patil, E. A. Ble-González, S. R. Isbel, S. M. Hampton and A. Bugarin, *Molecules*, 2022, **27**, 6575.
13 G. Wang, S. Sun and H. Guo, *Eur. J. Med. Chem.*, 2022, **229**, 113999.
14 F. Grande, G. Ioele, A. Caruso, M. A. Occhiuzzi, H. El-Kashef, C. Saturnino and M. S. Sinicropi, *Appl. Sci.*, 2022, **13**, 349.
15 C.-H. Chen, C.-S. Liu, X.-M. Guo, J.-P. Tong, J. Huang, T.-T. Shi and J. Sun, *J. Mol. Struct.*, 2024, **1306**, 137891.

16 D. Ling, C. Xiang, H. Guolin, S. Huisheng and N. Xiaohua, *3 Biotech*, 2025, **15**, 111.
17 S. Drygała, M. Radzikowski and M. Maciejczyk, *Front. Pharmacol.*, 2024, **15**, 1489657.
18 H. Elimam, Z. Hassan, N. A. A. Alhamshry, K. M. El-Say and A. M. A. Akabawy, *Naunyn-Schmiedeberg's Arch. Pharmacol.*, 2025, **15**, DOI: 10.1007/s00210-025-04356-9.
19 H. Şahin, A. Arslantürk Bingül, İ. Şengül and M. Bingül, *Istanb. J. Pharm.*, 2023, **53**, 39–44.
20 F. Grande, G. Ioele, A. Caruso, M. A. Occhiuzzi, H. El-Kashef, C. Saturnino and M. S. Sinicropi, *Appl. Sci.*, 2022, **13**, 349.
21 M. I. Abdjan, N. S. Aminah, A. N. Kristanti, I. Siswanto, A. L. L. Windah, T. M. Thant, R. Ramadhan, Y. Takaya, Z. Ul-Haq and M. I. Choudhary, *Eng. Sci.*, 2024, **31**, DOI: 10.30919/es1286.
22 İ. Çapan, M. Hawash, M. T. Qaoud and N. Jaradat, *ACS Omega*, 2025, **10**, 848–861.
23 B. Donarska, K. Seklecka, J. Cytarska, K. Piechowska, P. Ledwon, S. Kula, P. Krawczyk, A. Baranowska-Łączkowska and K. Z. Łączkowski, *Int. J. Mol. Sci.*, 2025, **26**, 7945.
24 S. S. Marufa, M. M. Rahman, M. M. Rahman, J. R. Debnath, M. A. Mim, R. Jahan, H. Nishino, M. S. Alam and M. A. Haque, *J. Mol. Struct.*, 2025, **1321**, 139861.
25 P. Krawczyk, B. Jędrzejewska, J. Cytarska, K. Seklecka and K. Z. Łączkowski, *Sensors*, 2024, **24**, DOI: 10.3390/s24196368.
26 S. Verma, P. Gupta, S. Lal, R. Narang, S. Mujwar, S. Saini and J. Sharma, *Eur. J. Med. Chem.*, 2025, **298**, 117995.
27 N. M. Hassanin, T. E. Ali, M. A. Assiri and S. M. Abdel-Kariem, *RSC Adv.*, 2024, **14**, 17245–17260.
28 C. Maccallini, R. Budriesi, B. De Filippis and R. Amoroso, *Int. J. Mol. Sci.*, 2024, **25**, 8486.
29 A. Mushtaq, U. Azam, S. Mehreen and M. M. Naseer, *Eur. J. Med. Chem.*, 2023, **249**, 115119.
30 J. Hughes, S. Rees, S. Kalindjian and K. Philpott, *Br. J. Pharmacol.*, 2011, **162**, 1239–1249.
31 M. Balouiri, M. Sadiki and S. K. Ibnsouda, *J. Pharm. Anal.*, 2016, **6**, 71–79.
32 M. A. Kumar, T. N. Minh An, I. J. Lee, S. Park and K. D. Lee, *Phosphorus Sulfur Silicon Relat. Elem.*, 2015, **190**, 1160–1168.
33 S. H. Ali and A. R. Sayed, *Synth. Commun.*, 2021, **51**, 670–700.
34 M. A. T. Nguyen, A. K. Mungara, J. A. Kim, K. D. Lee and S. Park, *Phosphorus Sulfur Silicon Relat. Elem.*, 2015, **190**, 191–199.
35 S. Cheenpracha, E.-J. Park, B. Rostama, J. M. Pezzuto and L. C. Chang, *Mar. Drugs*, 2010, **8**, 429–437.
36 V. Kumar, O. Prakash, S. Kumar and S. Narwal, *Pharmacogn. Rev.*, 2011, **5**, 19.
37 N.-H. Nguyen, N.-M.-A. Tran, T.-H. Duong and G. Van Vo, *RSC Adv.*, 2023, **13**, 8190–8201.
38 H. H. Nguyen, N. M. A. Tran, T. H. T. Nguyen, H. C. Vo, C. H. Nguyen, T. H. A. Nguyen, N. H. Nguyen and T. H. Duong, *J. Saudi Chem. Soc.*, 2022, **26**, 101489.
39 G. Van Vo, T. H. T. Nguyen, T. P. Nguyen, T. H. T. Do, N. M. A. Tran, H. T. Nguyen and T. T. Nguyen, *Saudi Pharm. J.*, 2022, **30**, 1301–1314.
40 N. D. T. Ha, T. Phuong and V. C. Nguyen, *ChemistrySelect*, 2023, **8**(17), e202300246.
41 G. Van Vo, T. H. T. Nguyen, T. P. Nguyen, T. H. T. Do, N. M. A. Tran, H. T. Nguyen and T. T. Nguyen, *Saudi Pharm. J.*, 2022, **30**(9), DOI: 10.1016/j.jsps.2022.06.018.
42 T. B. N. Dao, T. M. T. Nguyen, V. Q. Nguyen, T. M. D. Tran, N. M. A. Tran, C. H. Nguyen, T. H. T. Nguyen, H. H. Nguyen, J. Sichaem, C. L. Tran and T. H. Duong, *Molecules*, 2021, **26**, 1–15.
43 T. T. Ngoc Mai, P. N. Minh, N. T. Phat, T. H. Duong, T. N. Minh An, V. S. Dang, N. Van Hue and M. D. Tri, *RSC Adv.*, 2024, **14**, 9326–9338.
44 T. N. M. An, N. Van Cuong, N. M. Quang, T. V. Thanh and M. Alam, *ChemistrySelect*, 2020, **5**, 6339–6349.
45 H. Yang, L. Sun, Z. Wang, W. Li, G. Liu and Y. Tang, *J. Chem. Inf. Model.*, 2018, **58**, 2051–2056.
46 S. A. Hollingsworth and R. O. Dror, *Neuron*, 2018, **99**, 1129–1143.
47 O. S. Faleye, B. R. Boya, J.-H. Lee, I. Choi and J. Lee, *Pharmacol. Rev.*, 2024, **76**, 90–141.
48 M. T. Sayed, S. A. Elsharabasy and A. Abdel-Aziem, *Sci. Rep.*, 2023, **13**(1), DOI: 10.1038/s41598-023-36705-0.
49 S. S. Borisevich, T. E. Aksinina, M. G. Ilyina, V. O. Shender, K. S. Anufrieva, G. P. Arapidi, N. V. Antipova, F. Anizon, Y. J. Esvan, F. Giraud, V. V. Tatarskiy, P. Moreau, M. I. Shakhparonov, M. S. Pavlyukov and A. A. Shtil, *Cancers*, 2024, **16**, 834.
50 A. A. Hassan, N. K. Mohamed, A. A. Aly, M. Ramadan, H. A. M. Gomaa, A. T. Abdel-Aziz, B. G. M. Youssif, S. Bräse and O. Fuhr, *Molecules*, 2023, **28**, 7951.
51 E. Kuzu, E. Arzuk, F. Karakuş, B. Kuzu and H. Genç, *Turk. J. Chem.*, 2025, **49**, 215–227.
52 L. T. H. Nguyen, D. H. Vu, M. Q. Pham, Q. A. Ngo and N. B. Vo, *RSC Adv.*, 2025, **15**, 2850–2861.
53 S. Fang, X. Huang, F. Cai, G. Qiu, F. Lin and X. Cai, *J. Steroid Biochem. Mol. Biol.*, 2024, **240**, 106478.
54 H.-F. Lin, Y.-C. Jiang, Z.-W. Chen and L.-L. Zheng, *RSC Adv.*, 2024, **14**, 16349–16357.
55 F. Esposito, N. Pala, M. Carcelli, S. T. Boateng, P. S. D'Aquila, A. Mariani, S. Satta, J. C. Chamcheu, M. Sechi and V. Sanna, *J. Enzyme Inhib. Med. Chem.*, 2023, **38**(1), DOI: 10.1080/14756366.2023.2236802.
56 Z. Soleimani, M. Mohammadi, M. Halimi, S. Safapoor, N. Dastyafteh, E. Safaie, S. Mojtabavi, M. A. Faramarzi, M. Bozorgi-Koushalshahi, B. Larijani, M. Mohammadi-Khanaposhtani and M. Mahdavi, *Sci. Rep.*, 2024, **14**, 18693.
57 F. T. Zahra, A. Saeed, A. Ahmed, H. Ismail, M. U. Ijaz and F. Albericio, *RSC Adv.*, 2023, **13**, 24988–25001.
58 Y. Khan, S. Khan, R. Hussain, A. Maalik, W. Rehman, M. W. Attwa, R. Masood, H. W. Darwish and H. A. Ghabbour, *Pharmaceuticals*, 2023, **16**, 1650.
59 I. A. Seliem, *RSC Adv.*, 2025, **15**, 32309–32327.
60 A. Kolarič, M. Kokot, M. Hrast, M. Weiss, I. Zdovc, J. Trontelj, S. Žakelj, M. Anderluh and N. Minovski, *Antibiotics*, 2021, **10**, 862.
61 R. J. Young, *Expet Opin. Drug Discov.*, 2023, **18**, 965–972.

62 S. Q. Pantaleão, P. O. Fernandes, J. E. Gonçalves, V. G. Maltarollo and K. M. Honorio, *ChemMedChem*, 2021, **17**(1), DOI: 10.1002/cmdc.202100542.
63 F. Wu, Y. Zhou, L. Li, X. Shen, G. Chen, X. Wang, X. Liang, M. Tan and Z. Huang, *Front. Chem.*, 2020, **8**, DOI: 10.3389/fchem.2020.00726.
64 J. Zhang, H. Li, Y. Zhang, J. Huang, L. Ren, C. Zhang, Q. Zou and Y. Zhang, *Briefings Bioinf.*, 2025, **26**(5), DOI: 10.1093/bib/bbaf533.
65 Y. Zhang, G. Zhang, T. Wang, Y. Chen, J. Wang, P. Li, R. Wang and J. Su, *ChemBioChem*, 2025, **25**(22), DOI: 10.1002/cbic.202400297.
66 H. Komura, R. Watanabe and K. Mizuguchi, *Pharmaceutics*, 2023, **15**, 2619.
67 A. M. Hassan, H. S. Gattan, A. A. Faizo, M. H. Alruhaili, A. S. Alharbi, L. H. Bajrai, I. A. AL-Zahrani, V. D. Dwivedi and E. I. Azhar, *Pharmaceuticals*, 2024, **17**, 1617.
68 W. Lu and M. J. Buehler, *Mater. Adv.*, 2025, **6**, 4267–4285.